**Master of Science**

# GRID CONVERGENCE INDEX ESTMATION OF LARGE EDDY SIMULATION FOR TURBULENT HEAT TRANSFER FLOW USING NEK5000

The Graduate School of

University of Ulsan

Department of Mechanical Engineering

**Khanh Hoan Nguyen**

# GRID CONVERGENCE INDEX ESTMATION OF
# LARGE EDDY SIMULATION FOR
# TURBULENT HEAT TRANSFER FLOW USING NEK5000

**Academic advisor: Professor Kyoungsik Chang**

**A Thesis**

**Submitted to**

**the Graduate School of University of Ulsan**
**In partial Fulfillment of the Requirements**
**for the Degree of**

**Master of Science**

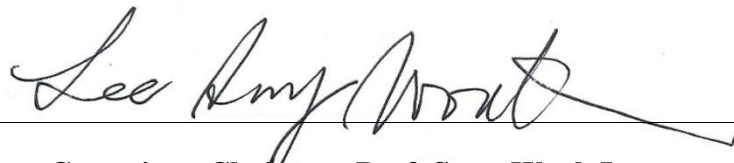**by**

**Khanh Hoan Nguyen**

**Department of Mechanical Engineering**
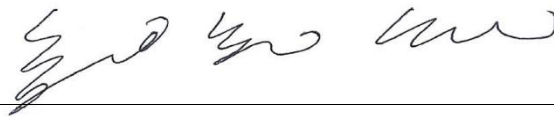**University of Ulsan, Republic of Korea**
**August 2021**

# GRID CONVERGENCE INDEX ESTMATION OF
# LARGE EDDY SIMULATION FOR
# TURBULENT HEAT TRANSFER FLOW USING NEK5000

**This certifies that the master thesis of Khanh Hoan Nguyen is approved.**

_____

**Committee Chairman Prof. Sang-Wook Lee**

_____

**Committee Member Prof. Kyoungsik Chang**

_____

**Committee Member Prof. Jichul Shin**

**Department of Mechanical Engineering**

**University of Ulsan, Republic of Korea**

**August 2021**

# Acknowledgment

Firstly, I would like to express my sincere gratitude to my Supervisor, Professor Kyoungsik Chang, for support me during the work on this thesis. He gave me an opportunity to successfully complete my master's course in Korea. His immense knowledge and plentiful experience have encouraged me in all the time of my academic research and daily life.

I am deeply grateful to my family who always believes in me and unwavering support for me. It would be impossible for me to complete my study if I do not have their understanding and encouragement in the past few years.

I would like to thank Ho van Thanh, Kim Byeong-Cheon, and Nguyen Ho Nghia for always help me with everything as my brothers. I learned more things from their sharing expertise, sincere and valuable guidance, and encouragement extended to me. I also thank other labmates in TTFL, Jung Youngki, Park Sanghwan, Bae Jaehyeon, Nguyen Hoai Thanh, and AFEL members, Cheng Kuiyu, Huynh Van Tinh. Their kind help and support have made my study and life in Korea a wonderful time.

In the end, I am also pleased to say thank you to all my friends, who provided stimulating discussions as well as happy distractions to rest my mind outside of my research.

Ulsan, June 2021

**NGUYEN KHANH HOAN**

i

# Abstract

# GRID CONVERGENCE INDEX ESTMATION OF LARGE EDDY SIMULATION FOR TURBULENT HEAT TRANSFER FLOW USING NEK5000

Large eddy simulation is performed in heat transfer of turbulent flow with NEK5000 code based on spectral element method to study uncertainty quantification by Grid Convergence Index. Two geometries are investigated including simple geometrical configurations, pipe flow, and more complex geometrical configurations, rod bundle flow.

The turbulent pipe flow with heat transfer is considered with Reynolds number $Re = 19,000$ and Prandtl number $Pr = 0.71$. Three meshes (fine, medium, and coarse) with the fixed interpolation polynomial order, 8 and three orders (4th, 6th, and 8th) of interpolation polynomial with the fine mesh are examined. The effects of different grid and interpolation polynomial order are studied to highlight the effectiveness of high order spectral element. The Grid Convergence Index using two modified versions from original Roache's GCI method are estimated based on simulation results. Two modified versions include the modification of Roache's GCI method described in the ASME V&V 20-2009 guideline and the simplified least square method version GCI. Though GCI estimation, it was found that the accuracy of the SLS – GCI method is better than that by Mod. – ASME.

The rod bundle simulation takes the advantage of the symmetries of the domain that can be divided into twelve homologous sections. The rod is chosen with the case of $P/D = 1.24$ with Reynold number $Re = 10,000$ and Prandtl number $Pr = 1.0$. Three meshes (fine, medium, and coarse) with the fixed interpolation polynomial order

of 7<sup>th</sup> order are examined to study quantify the uncertainty by GCI estimation with SLS – GCI method.

# Contents

# List of Figures

# List of Tables

# Abbreviations

| | |
|---|---|
| CFD | Computational fluid dynamics |
| SEM | Spectral element method |
| FEM | Finite element method |
| GLL | Gauss – Lobatto - Legendre |
| LES | Large eddy simulation |
| DNS | Direct numerical simulation |
| UQ | Uncertainty quantification |
| GCI | Grid convergence index |
| Mod. – ASME | Modification of Roache's GCI method |
| SLS – GCI | Simplified Least Square version GCI estimation method |

# Chapter 1. Introduction

## 1.1 Overview

The examination of the spatial convergence is important issue in a simulation to determine the error discretization order. The simulation on two or more finer mesh are required for this method. While the grid and time step are refined the spatial and temporal discretization errors, respectively, should asymptotically approaches zero. The solution of the discrete method in the choice of finite time and space resolution appears discretization error. To estimate discretization error, Roache (1998) [1] provides a discretization error estimation, the Grid Convergence Index (GCI) methodology as a procedure to determine and report discretization errors estimation in the CFD simulation. The GCI permits the uncertainty quantification (UQ) due to discretization grid. This method is based on a grid refinement error estimator derived from the generalized Richardson's extrapolation (Richardson 1908, 1927) [2, 3].

The Roache's GCI estimation is a method popular in the CFD, as a traditional method of the estimating discretization error, however, the constructed grids should be a constant grid refinement ratio. To overcome the drawback of the traditional method, there are the two modified method from Roache's GCI method (Roache, 1994 and 1997) introduced in the ASME guideline (ASME,2009) [4], the modified ASME V&V 20 (mod. -ASME), and the least square version GCI method that is developed by Eca and Hoeksta (2006) [5], the simplified lest square version GCI (SLS – GCI). The T – pipe problem with three different mesh arrangements at common boundary condition is examined by Tanaka and Miyake (2015) [6] to prove the effectiveness of the above two GCI methods.

Uncertainty quantification (UQ) in the computational fluid dynamics (CFD) field has been a hot issue, with various attempts to quantify the uncertainty and obtain the statistical

distribution of a quantity of interest (QoI) based on CFD results. Among various methods for UQ in CFD, the polynomial chaos expansion (PCE)-based method is able to produce predictions as highly accurate as the previous sample-based Monte Carlo method and can save computational time and cost. One often-used PCE-based method is the intrusive polynomial chaos approach, which is based on the stochastic Galeskin method. The SEM methodology is considered a promising alternative for UQ of CFD, since SEM is able to consider probabilistic input based on the given basis function and can produce highly accurate results with fewer grid points.

Nowadays, computational fluid dynamic is becoming common and important in the industrial process. Turbulent heat transfer flow is an important problem in CFD and extensively investigated in engineering application such as nucleating reactor, combusting chambers, etc. The problems that are mainly focused on the control of turbulent characteristics with effect of heat is a challenge. Many studies make to examine the effect of different Prandtl number and Reynolds numbers on turbulent heat transfer flow. Tavakoli et al. (2014) [7] performed turbulent heat transfer in circular pipe flow using large eddy simulation for a frictional Reynolds number, $Re_\tau = 180$, and the low Prandtl number which ranged from 0.1 to 1.0. The statistical analysis of the probability density functions (PDFs) for the Nusselt number for different Prandtl numbers are also presented. The LES for the turbulent heat transfer in pipe flow at the different Prandtl number larger than 0.71 and for high Reynold numbers up to 20,000 is presented by Ould-Rouiss, Bousbai, and Mazouz (2013) [8]. The fully developed turbulent channel flow using direct numerical simulation with the use of the finite difference method and the three Reynolds numbers ($Re_\tau =$180,395, and 640) by Hiroyuki Abe et al. (2001) [9].

Recently, increase of computing powers is able to hand on numerical simulation with

high accuracy and with the timely response of the current requests. Introduced by Patera, A.T in 1984 [10], spectral element method is a combination of the generality of finite element methods with the high accuracy of the spectral techniques that uses high order piece wise polynomials as basic functions. In SEM, the domain is divided by the hexahedral spectral elements and the solutions is defined by Legendre polynomials at the Gauss – Lobatto – Legendre (GLL) quadrature points. Legendre polynomials is a family of high – order orthogonal polynomials. Thus, SEM has large of local computational work at each element and only the global work as boundary condition and pressure coupling on the global mesh. The open – source – based SEM, Nek5000, is developed by Fischer, Lottes, and Kerkemeier (2008) [11]at the Argonne National Laboratory (ANL, US Dept. of Energy) with purpose to overcome the current drawback of the standard CFD solvers. Nek5000, is written by Fortran and C, used portable message passing interface (MPI) platform for parallel calculation is able to scale up to millions of processors. The accuracy and computability of SEM with Nek5000 are proven along to studies. The spectral element code Nek5000 has been used for DNS and LES techniques. In the study of Khoury et al. (2013) [12] the fully developed DNS in turbulent pipe flow at moderately high frictional Reynolds numbers up to $Re_\tau$ =1,000, the solutions are compared with previous studies and showed that a high – order polynomial is necessary for accuracy with high Reynold number simulation. The inhomogeneous heat flux on the pipe wall via DNS based on SEM to calculate turbulent forced convection in the report of Antoranz, A et al. (2015) [13]. LES technique with SEM is performed by Ryzhenkov et al. (2016) [14] for the turbulent heat transfer in channel flow at $Re = 6,800$ and compared the value of friction velocity and temperature indicating the near wall solution accuracy with 2% accuracy interval, even 30 times fewer grid point than DNS. Nek5000 is able to work well in more complex geometries and provide reliable results in compound boundary condition problem requiring

high precision. Zhixin Wang and Yongmann M. Chung (2018) [15] perform a DNS of a turbulent $90^0$ bend pipe flow with long straight pipe section 40D. The Reynold number in pipe flow is $Re = 5,300$ and bend curvature is $\gamma = 0.4$. Rod bundles, which is an essential component of nuclear power plant, is presented by Javier Martínez el at. (2019) [16]. The simulation uses LES of a small section of a single rod with $P/D$ of 1.12 and 1.24. The Nek5000 steady state solver is chosen for solving the temperature field in the pseudo – RANS approach.

## 1.2 Research object

The aim of this thesis focuses on large eddy simulation in the turbulent flow under heat transfer using the open source, Nek5000, based on spectral element method with two geometries, the simple geometrical configuration of the pipe flow and more complex geometrical configuration of the rod bundle flow. The turbulent heat transfer in pipe flow is an important problem in engineering applications such as heat exchangers, combustion chambers, etc. On the other hands, the rod bundles are an essential component in the nuclear power plants. Moreover, the two modified methods from Roache's GCI method are considered to measure the percentage difference between the numerical value and the asymptotic value, as well as indicate changes in the solution.

Heat transfer in a fully developed turbulent pipe flow is considered by Reynolds number, $Re = 19,000$, and Prandtl number, $Pr = 0.71$. The flow of an incompressible viscous fluid is examined in a smooth circular pipe with a diameter, $D$, and axial length, $L = 10D$. The results of three different grid levels and three polynomial orders of the spectral elements are showed to study the effect of grid levels and polynomial orders to accuracy of the solution. From that, the accuracy of the solution in spectral element method with effect of polynomial order or grid level are shown. Two GCI method are mod. –

ASME and SLS – GCI used to measure the percentage difference between the numerical value and the asymptotic value, as well as indicate changes in the solution when the grid is further refined, and the polynomial order is increased or decreased in spectral element method.

The bare rod cases have been chosen with $P/D = 1.24$ and $L_z = 2\pi D$ with the Reynold number, $Re = 10,000$ and the Prandtl number of the fluid, $Pr = 1.0$. The periodic boundary condition is applied in vertical direction. To reduce the computing cost, one may take advantage of the symmetries of the domain. The three difference grid levels are considered with the fixed polynomial order of $7^{th}$ order. The SLS – GCI is chosen for GCI estimation in this case with three gird levels arrangement due to the GCI estimation results of the pipe flow simulation show that the accuracy of the estimate by SLS – GCI is greater than that by Mod. – ASME.

## 1.3 Thesis Outline

This thesis is divided in 5 chapters. The first chapter is a brief introduction to relevant studies and subjects. The second chapter summaries the governing equation, the numerical method, and the formulation of the grid convergence index estimation. The third and fourth chapters shows the results of pipe flow and rod bundle flow calculation. The last chapter implies the conclusions, and future works.

# Chapter 2. Governing equation and Numerical Methods

In this chapter, the numerical method used in the present work is explained. Grid convergence index (including Roach's method, ASME. - mod method and SLS – GCI method) are explained below.

## 2.1 Governing equations

Time dependent Navier – Stokes equation with the assumption of incompressible flow and advection diffusion equation for thermal field are shown below,

$$\frac{\partial \boldsymbol{u}}{\partial t} + \boldsymbol{u} \cdot \nabla \boldsymbol{u} = -\nabla p + \frac{1}{Re}\Delta \boldsymbol{u}, \qquad \nabla \cdot \boldsymbol{u} = 0, \qquad (2.1.1)$$

$$\frac{\partial \theta}{\partial t} + \boldsymbol{u} \cdot \nabla \theta = \frac{1}{RePr}\Delta \theta, \qquad (2.1.2)$$

where $\boldsymbol{u}$, $p$, and $\theta$ are the dimensionless velocity, pressure, and temperature, respectively. The Reynolds number $Re = \rho \boldsymbol{u} D / \mu$ is defined using the mean velocity of the fluid $\boldsymbol{u}$, the density $\rho$, the diameter of the pipe $D$, and the dynamic viscosity of the fluid $\mu$. The Prandtl number $Pr = c_p \mu / k$ is the ratio of convection diffusivity and conduction diffusivity, where $c_p$ is specific heat, and k is thermal conductivity.

The open-source spectral element code, NEK5000, which was developed by Fischer et al. [11] at the Argonne National Laboratory (U.S. Dept. of Energy), solves incompressible Navier–Stokes equations analyzed as Lagrangian interpolations based on Gauss – Lobatto – Legendre points. The velocity space is approximated by typical $N^{\text{th}}$ – order Lagrangian polynomial interpolations on the GLL points, and pressure space employs $N$ or $N-2$ order of Lagrangian interpolants on the Gauss–Legendre quadrature points, which herein was $P_N - P_N$ or $P_N - P_{N-2}$ as proposed by Maday and Patera [17]. The time integration scheme in NEK5000 uses a semi-implicit method, with the viscous terms treated implicitly by a $k$-order backward differentiation (BDF$k$), and the non-linear terms explicitly by a $k$-

order extrapolation (EXT$k$) treatment with detail in section (2.1.2).

In this thesis, since the considered Reynolds number in both geometries is high. Direct Numerical Simulation is not feasible for problems of a certain geometrical complexity due to a high computational memory and cost. Large eddy simulation is an attractive alternative (shown in section 2.2) which is cheaper than DNS.

### 2.1.1 Boundary conditions

Based on the geometry and flow types, the different boundary conditions are applied. The mathematical formulation and physical interpretation of boundary conditions for velocity and temperature fields are used in this thesis as below,

- The wall boundary condition ("W") is known as the no – slip condition, mathematically this is equivalent to homogeneous Dirichlet conditions, $\boldsymbol{u} = 0$.

- The periodic boundary condition ("P") corresponds to $\boldsymbol{u}(x) = \boldsymbol{u}(x + L)$, where $L$ is the periodic length.

- The symmetric boundary condition ("SYM") is defined with formular by the normal vector, $\boldsymbol{n}$, and the tangent vector, $\boldsymbol{t}$, as below,

$$\boldsymbol{u} \cdot \boldsymbol{n} = 0, \tag{2.1.3a}$$

$$(\nabla \boldsymbol{u} \cdot \boldsymbol{t}) \cdot \boldsymbol{n} = 0, \tag{2.1.3b}$$

- In the thermal field, the temperature boundary condition ("t") is standard Dirichlet boundary condition.

### 2.1.2 Time discretization

The order of time discretization is important for accuracy and stability of solution. The temporal discretization which is widely used in Nek5000 is backward differentiation and extrapolation of order k (BDF$k$/ EXT$k$) scheme.

Considering a simple equation of the form $dy/dt = f(y)$. The kth order implicit backward differentiating scheme is based Taylor expansion, the BDF$k$ scheme is given by,

$$\frac{1}{\Delta t}\sum_{i=0}^{k}\beta_i y^{n+1-i} \approx f(y^{n+1}) \tag{2.1.4}$$

where $\{\beta\}_{i=0}^{k}$ are BDF coefficients and $\Delta t$ is the time step size. The number of implicit relations to be solved are the same for different orders $k$. In the Navier – Stokes discretization, there are difficult to solve when treated implicitly creates non – symmetric, non – linear system. While the explicit method uses the implements high order extrapolation on the non – linear terms including the advection part. The $k^{\text{th}}$ order extrapolation (EXT$k$) of a general nonlinear term $f(y^{n+1})$ is given by,

$$f(y^{n+1}) \approx \sum_{i=1}^{k}\alpha_i f(y^{n+1-i}) \tag{2.1.5}$$

where $\{\alpha_i\}_{i=1}^{k}$ is a set of extrapolation coefficients corresponding to the specific order of the scheme. From equation (2.1.4) and (2.1.5), Adding the BDF$k$ and EXT$k$ schemes together result in the BDF$k$/ EXT$k$ scheme,

$$\frac{1}{\Delta t}\sum_{i=0}^{k}\beta_i y^{n+1-i} \approx \sum_{i=1}^{k}\alpha_i f(y^{n+1-i}) \tag{2.1.6}$$

In Nek5000, the second and third order BDF$k$/EXT$k$ schemes is considered for the time integration schemes with the viscous terms treated implicitly by a $k$-order backward differentiation (BDF$k$), and the non-linear terms explicitly by a $k$-order extrapolation (EXT$k$).

### 2.1.3 Interpolating Polynomial

The two families that are most relevant in the context of the spectral element method are the Legendre polynomials and the Lobatto polynomial. Legendre polynomials, denoted by $L_n(x)$, are orthogonal with respect to the flat integration weight $w(x) = 1$ and the integration interval $[-1, 1]$. The Legendre polynomials are explicitly given by,

$$L_n(x) = \frac{1}{2^n n!} \frac{d^n}{dx^n} (x^2 - 1)^n \tag{2.1.7}$$

And the Legendre polynomial satisfy the differential equation,

$$\frac{d}{dx}\left[(x^2 - 1)\dot{L}_n(x)\right] = n(n+1)L_n(x) \tag{2.1.8}$$

The Lobatto polynomials, denoted by $Lo_n(x)$, are orthogonal with respect to the integration weight $w(x) = (1 - x^2)$ and the integration interval $[-1, 1]$. The Lobatto polynomial are defined in terms of the Legendre polynomial,

$$Lo_n(x) = \dot{L}_{n+1}(x) \tag{2.1.9}$$

The Lobatto polynomials satisfy the differential equation,

$$\frac{d}{dx}\left[(x^2 - 1)Lo_{n-1}(x)\right] = n(n+1)L_n(x) \tag{2.1.10}$$

Given a set of $n + 1$ data points $x_i$. The $N^{\text{th}}$ degree Lagrange Polynomial Interpolation have a form,

$$l_i^{(N)}(x) = \prod_{k=1, k \neq i}^{N+1} \frac{x - x_k}{x_i - x_k}, \quad i = \overline{1, N+1} \tag{2.1.11}$$

For $j = 1, 2, \ldots, N + 1$, the cardinal interpolation property,

$$l_{N,i}(x_j) = \begin{cases} 0, & if\ i \neq j \\ \delta_{ij}, & if\ i = j \end{cases} \tag{2.1.12}$$

where $\delta_{ij}$ is Kronecker's delta representing the identity matrix. The interpolating polynomial can be expressed in terms of the Lagrange polynomial as,

$$P_N(x) = \sum_{i=1}^{N+1} f(x_i) l_{N,i}(x) \tag{2.1.13}$$

From that, to satisfies the property (2.1.8) and requirement of the interpolating polynomial condition,

$$P_N(x) = \sum_{i=1}^{N+1} f(x_i) L_{N,i}(x) = \sum_{i=1}^{N+1} f(x_i) \delta_{ij} = f(x_i) \tag{2.1.14}$$

Replacement of the $N^{\text{th}}$ degree Lagrange interpolating polynomial emerges by $N + 1$

17

degree generating polynomial, which is 0 at all data points,

$$\Phi_{N+1}(x) = \prod_{i=1}^{N+1}(x - x_i) \tag{2.1.15}$$

Straightforward differentiation of (2.1.11) and substituting the results into (2.1.7) can be rewrite as the form,

$$L_{N,i}(x) = \frac{1}{x - x_i}\frac{\Phi_{N+1}(x)}{\dot{\Phi}_{N+1}(x_i)} \tag{2.1.16}$$

is the $i^{\text{th}}$ Lagrange interpolation polynomial.

Without loss of generality, we restrict our attention to the interval $[-1, 1]$. For a given set of collocation points $x_i$ with $i = 1,2, ..., N + 1$. The collocation point distribution is such that the $N - 1$ optional conditions are satisfied for the internal nodes,

$$\dot{l}_{N,i}(x_i) = 0 \tag{2.1.17}$$

The internal node points as the roots of the Lobatto polynomial $Lo_{N-1}(x)$. The second derivative of the generating polynomial, $\Phi_{N+1}(x)$ vanishes at the node points $x_i$, with $i = 2,3, ..., N$, i.e $\ddot{\Phi}_{N+1}(x_i) = 0$, thus,

$$\ddot{\Phi}_{N+1}(x) = c\frac{\Phi_{N+1}(x)}{(x - 1)(x + 1)} = -c\frac{\Phi_{N+1}(x)}{(1 - x^2)} \tag{2.1.18}$$

where $c$ is a constant. The coefficient of the highest power monomial $x^{N+1}$ of $\Phi_{N+1}$ is equal to 1. This implies $c = N(N + 1)$, therefore, the generating polynomial satisfies the differential equation,

$$(1 - x^2)\ddot{\Phi}_{N+1}(x) + N(N + 1)\Phi_{N+1}(x) = 0 \tag{2.1.19}$$

The completed Lobatto polynomial is defined as,

$$Lo_{n-1}^c(x) = (1 - x^2)Lo_{n-1}(x) \tag{2.1.20}$$

They are commonly referred to as Gauss – Lobatto – Legendre points (GLL points). Figure 1 shows the Lagrange polynomial of degree $4^{\text{th}}$, $6^{\text{th}}$, and $8^{\text{th}}$ with GLL points as

collocation points.
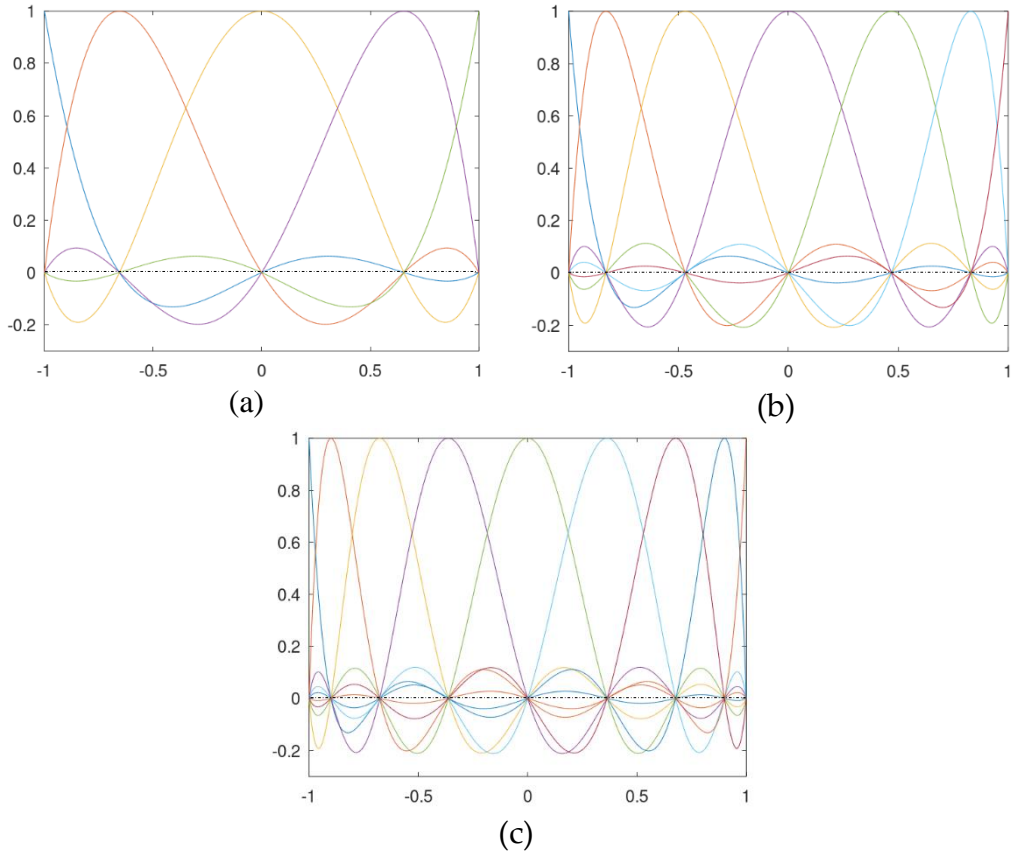


**Figure 1** *The Lagrange polynomials of degree 4$^{th}$ (a); 6$^{th}$ (b); and 8$^{th}$ (c). The collocation points, indicated by vertical lines, are the Gauss – Lobatto – Legendre (GLL) points.*

Nek5000 provides some basic tools for generation of mesh, genbox. This tool cannot handle with more complex geometries. An automatic way of converting a mesh created from .msh file to the format required by Nek5000 is msh2nek. The way the mesh is created in this thesis is shown in figure 2.
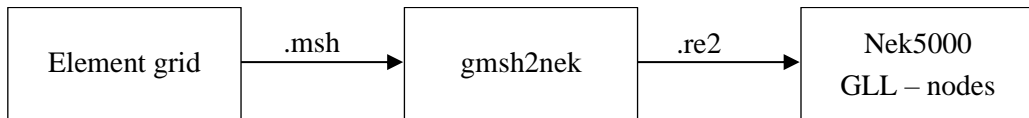


**Figure 2** *The way to generate the mesh.*

In this thesis, the elemental mesh is generated by python code and gmsh, the msh2nek tool converts this to a .re2 file and after that the GLL – nodes are distributed by the initialization in Nek5000.

## 2.2 Large eddy simulation models

Even though DNS is able to resolve turbulent quantities correctly without any model, this methodology requires high computational memory and cost. LES is one of most powerful tools for simulating turbulent flows.

The filtered Navier – Stokes can be written ("Nek5000 note" 2005 [18]) as below,

$$\frac{\partial \bar{\boldsymbol{u}}}{\partial t} + (\bar{\boldsymbol{u}} \cdot \nabla)\bar{\boldsymbol{u}} = -\nabla \bar{p} + \frac{1}{Re}\Delta\bar{\boldsymbol{u}} - \nabla \cdot \tau, \qquad \nabla \cdot \bar{\boldsymbol{u}} = 0, \qquad (2.2.1)$$

$$\frac{\partial \bar{\theta}}{\partial t} + (\bar{\boldsymbol{u}} \cdot \nabla)\bar{\theta} = \frac{1}{RePr}\Delta\bar{\theta} - \nabla \cdot q, \qquad (2.2.2)$$

where overbar denotes the filtered (or resolved) field that is computed on the computational grid, $\bar{\boldsymbol{u}}(x,t) = \int G(x-r)\boldsymbol{u}(r,t)dr$ with the filter function $G$. The extra stress term $\tau = \overline{\boldsymbol{u} \cdot \boldsymbol{u}} - \bar{\boldsymbol{u}} \cdot \bar{\boldsymbol{u}}$ is the sub – grid stress tensor and $q = \overline{\boldsymbol{u}\theta} - \bar{\boldsymbol{u}}\bar{\theta}$ is the sub – grid heat flux vector.

The sub – grid stress tensor and sub – grid heat flux vector can be expressed as follows:

$$\tau_{ij} - \frac{\delta_{ij}}{3}\tau_{kk} = -2(C_s\Delta)^2|\bar{S}|\bar{S}_{ij}, \qquad (2.2.3)$$

$$q_i = -r_t^{-1}(C_s\Delta)^2|\bar{S}|\partial_i\bar{\theta}, \qquad (2.2.4)$$

$$\bar{S}_{ij} = \frac{1}{2}(\partial_j\bar{u}_i + \partial_i\bar{u}_j), \qquad (2.2.5)$$

where $\delta_{ij}$ is the Kronecker delta, $C_s$ and $r_t$ are the Smagorinsky coefficient and turbulent diffusivity, respectively, $\Delta$ is the filter width, and $\bar{S}_{ij}$ is the strain-rate tensor which has a norm $|\bar{S}| = (2\bar{S}_{ij}\bar{S}_{ij})^{1/2}$. The Smagorinsky coefficient and turbulent diffusivity are defined as:

$$C_s^2 = \frac{\langle(\hat{\bar{u}}_i\hat{\bar{u}}_j - \widehat{\bar{u}_i\bar{u}_j})\rangle}{\langle 2\left(\hat{\Delta}^2\left|\hat{\bar{S}}\right|\hat{\bar{S}}_{ij} - \Delta^2\widehat{|\bar{S}|\bar{S}_{ij}}\right)\bar{S}_{ij}\rangle}, \qquad (2.2.6)$$

$$r_t = C_s^2 \left[ \frac{\langle \left( \hat{\bar{u}}_i \bar{\theta} - \widehat{\bar{u}_i \bar{\theta}} \right) \rangle}{\langle 2 \left( \hat{\Delta}^2 \left| \hat{\bar{S}} \right| \partial_i \hat{\bar{\theta}} - \Delta^2 \overline{|\bar{S}| \partial_i \bar{\theta}} \right) \partial_i \bar{\theta} \rangle} \right]^{-1} , \qquad (2.2.7)$$

where $\langle \cdot \rangle$ denotes a spatial averaging procedure along the homogeneous direction of the flow.

## 2.3 Grid convergence index

One important issue in CFD simulations is which grid level is appropriate to obtain the most reasonable results. To determine this, a grid refinement study to assess the effect of the grid resolution is necessary, and quantitative measurement according to the grid refinement study should be addressed. We therefore proposed a GCI estimation based on grid refinement to quantitatively represent the results of the grid test. This method involves performing the simulation on two or more successively finer grids. The GCI computes a percentage error between the numerical solution and the asymptotic value and indicates how the solution will change with a further refinement of the grid. Basically, two grid levels are required to calculate GCI, but three grid levels are recommended for accurate estimation of the order of convergence. Three meshes were constructed with the grid refinement factors, defined as $r_{12} = h_2/h_1$ and $r_{23} = h_3/h_2$, where $h_1 < h_2 < h_3$ is the representative cell size and the value $f_k$ at the corresponding grid level ($k = 1,2,3$) is normalized by an appropriate representative value.

In this section, three GCI estimation methods are introduced, including Roache's original GCI method, the modified methods from the Roache's GCI method described in the ASME V&V – 20 guidelines (Mod. - ASME) [4], and the Eca – Hoekstra 's least square version GCI (was named Simplified least square version GCI estimation method, SLS– GCI) [6].

### 2.3.1  Roache's GCI method

Roache (1998) [1] has provided a method based on a grid refinement error estimator

derived from the generalized Richardson's extrapolation (Richardson 1908, 1927) [2, 3]. Roache's GCI method can be used to calculate a higher-order estimate of the flow field from a series of lower-order discrete values.

The order of accuracy can be obtained from three solutions using a constant grid refinement ratio $r$,

$$p = ln\left(\frac{f_3 - f_2}{f_2 - f_1}\right)/ln\,(r). \tag{2.3.1}$$

The Richardson extrapolation is able to be generalized by introducing a $p^{th}$ order method and $r$ value of the grid refinement ratio as:

$$f_{h=0} = f_1 + \frac{f_1 - f_2}{r^p - 1}. \tag{2.3.2}$$

The GCI provides an estimation of the discretization error in the finest grid solution relative to the converged numerical solution. The GCI on the finest grid is defined as:

$$GCI_{fine} = \frac{F_s|\varepsilon|}{r^p - 1}, \tag{2.3.3}$$

where $F_s$ is a safety factor (it is recommended to be $F_s = 3$ if two grids are compared, and $F_s = 1.25$ if three or more grids are compared); $\varepsilon = (f_2 - f_1)/f_1$ is the relative error.

In engineering design or analysis requiring many CFD simulations, the coarser grid might be desirable. Thus, it is necessary to evaluate the error for the coarser gird. In this case the GCI in the coarse mesh is defined as:

$$GCI_{coarse} = \frac{F_s|\varepsilon|r^p}{(r^p - 1)}. \tag{2.3.4}$$

It is important that each grid level yield solutions that are in the asymptotic range of convergence for the computed solution. This can be checked by observing two GCI values as computed over three grids,

$$GCI_{coarse} = r^p GCI_{fine}. \tag{2.3.5}$$

Roache's GCI method has a simple formula, and it is easy to estimate the GCI.

However, in the original method the accuracy order is computed by the logarithmic function of the differences of the $f_k$ value. Thus, the value of $f_k$ needs to increase or decrease commensurately with a constant refinement ratio (i.e., $f_1 < f_2 < f_3$ or $f_1 > f_2 > f_3$). Besides that, requiring a constant grid refinement ratio, over three meshes, can become a computational burden, especially for three dimensional problems.

### 2.3.2 Modified ASME V&V 20 method

A modified method was introduced in the ASME V&V 20-2009 guideline (ASME 2009) [4], based on Roache's original method, to overcome the deficiency described immediately above. We arranged three meshes for estimation of the GCI value, and the observed order of convergence $\hat{p}$ was estimated as:

$$\hat{p} = \frac{ln\left[\frac{\varepsilon_{32}}{\varepsilon_{21}} + q(\hat{p})\right]}{ln(r_{21})}, \tag{2.3.6}$$

$$\varepsilon_{32} = f_3 - f_2, \varepsilon_{21} = f_2 - f_1 \tag{2.3.7}$$

$$q(\hat{p}) = ln\left(\frac{r_{21}^{\hat{p}} - s}{r_{32}^{\hat{p}} - s}\right), \tag{2.3.8}$$

$$s = 1 \times sign\left\{\frac{\varepsilon_{32}}{\varepsilon_{21}}\right\}. \tag{2.3.9}$$

When $r_{21} \neq r_{32}$, the convergence order $\hat{p}$ is calculated iteratively with $q(\hat{p})$. If the rate of mesh refinement is constant, this iteration step can be skipped. $\hat{p}$ can take the value of less than one even though the higher-order scheme is used. Moreover, for simple laminar flow problems, $\hat{p}$ nearly equals zero. A lower threshold must be introduced for the observed $\hat{p}$, and the order of convergence $p$ is defined as:

$$p = max(p_l, \hat{p}). \tag{2.3.10}$$

where $p_l$ is the lower threshold of the order [17,18], as the lowest order of accuracy of the discretization schemes ($p_l = 1$). The GCI value $u_{GCI}$ and the extrapolated value $f_c$ can be

defined as:

$$f_c = \frac{r_{21}^p f_1 - f_2}{r_{21}^p - 1}, \tag{2.3.11}$$

$$u_{GCI} = \frac{F_s \times |f_2 - f_1|}{r_{21}^p - 1} = F_s \times |f_c - f_1|, \tag{2.3.12}$$

Here, $F_s$ is a safety factor. Although $F_s = 1.25$ is recommended in the ASME guideline, in this case $F_s$ is varied according to the convergence order $p$. If $p_l < p \leq p_u$, then $F_s = 1.25$ is applied. Otherwise, $F_s = 3.0$ is applied as a conservative value. The upper threshold of the order $p_u$ ($= 2.0$) is the highest order of accuracy of the discretization scheme (Tanaka, Ohshima, and Monji 2009, 2010) [19, 20].

The Mod. – ASME method is more accurate than the original method. However, it would be convergence problematic if the grid refinement factors did not have a constant rate, and the iteration step needs to be solved to determine the observed order of convergence.

### 2.3.3  Simplified least square version GCI

The simplified least square version GCI (SLS—CGI) was proposed by Tanaka and Miyake (2015) [5] based on the least square CGI method by Eca and Hoeska (2006) [6]. To estimate the order of convergence, the original method requires the numerical values for many more than three different meshes ($k > 3$), whereas the SLS–GCI method is devised to work with three numerical values in different meshes ($k = 3$), the minimum number to reduce the cost.

In SLS–GCI, the convergence order $p$, the extrapolated value $f_c$, and coefficient α are computed by the least square method following these equations:

$$\hat{f}_k = f_c + \alpha(h_k)^p, \tag{2.3.13}$$

$$S = \sum_{k=1}^{3} [f_k - (f_c + \alpha(h_k)^p)]^2, \tag{2.3.14}$$

As a result, the GCI value $u_{GCI}$ and the error of estimation between the numerical and estimated results $u_e$ can be computed accordance with the order of convergence $p$:

- Case 1, $p_l < p$

$$u_{GCI} = \frac{F_s \times |\hat{f}_2 - \hat{f}_1|}{r_{21}^p - 1} = F_s \times |f_c - f_1|, u_e = \sqrt{\frac{1}{3} \sum_{k=1}^{3} [f_k - (f_c + \alpha h_k^p)]^2} \tag{2.3.15}$$

If $p > p_u$, $F_s = 3.0$ is applied. Otherwise, $F_s = 1.25$ is applied.

- Case 2, $0 < p < p_l$, $p = p_l = 1$

$$u_{GCI} = \frac{3.0|\hat{f}_2 - \hat{f}_1|}{r_{21}^p - 1}, u_e = \sqrt{\frac{1}{3} \sum_{k=1}^{3} [f_k - (f_c + \alpha h_k^p)]^2} \tag{2.3.16}$$

In this case, $p$ is set to $p_l$, then the coefficient $\alpha$ and the extrapolated value $f_c$ must be re-estimated according to Equation (2.3.13) and (2.3.14).

- Case 3, $p \leq 0$ or $p$ is not converged, then:

$$u_{GCI} = 0, u_e = \sqrt{\frac{1}{3} \sum_{k=1}^{3} (f_k - f_c)^2}, f_c = \frac{1}{3} \sum_{k=1}^{3} f_k \tag{2.3.17}$$

The strength of SLS–GCI is to reduce the cost of verification and validation and to achieve accuracy similar to the two above methods. Nevertheless, the formula of this method is quite complicated.

### 2.3.4 Combination of Uncertainties

The global GCI $u_{GCI}$ is estimated by the root mean square (RMS) function with respect to the local GCI as

$$U_{GCI} = \sqrt{\frac{1}{M}\sum_{j=1}^{M}\{(u_{GCI})_j\}^2} \qquad\qquad (2.3.18)$$

The index of $\varepsilon_c$ estimated by the RMS of the differences between the reference result $f_0$ (e.g., experimental, and analytical results) and the extrapolation result $f_c$ is also an uncertainty factor. The index of $\varepsilon_c$ estimated is estimated as follows:

$$\varepsilon_c = \sqrt{\frac{1}{M}\sum_{j=1}^{M}\{|(f_0)_j - (f_c)_j|\}^2} \qquad\qquad (2.3.19)$$

Moreover, for the SLS-GCI, the local error of estimation $u_e$ is counted as an uncertainty factor, as follows:

$$U_e = \sqrt{\frac{1}{M}\sum_{j=1}^{M}\{(u_e)_j\}^2} \qquad\qquad (2.3.20)$$

Therefore, the combined standard uncertainty $U_S$ of the numerical discretization as the over-all value in the domain can be estimated by the root sum square (RSS) function regarding the global values of the GCI of $U_{\mathrm{GCI}}$ with a modification coefficient of 1.15 to fit the value to the standard deviation, the error of estimation $U_e$, and the difference $\varepsilon_c$ between the extrapolation and the reference:

$$U_S = \sqrt{\left(\frac{U_{GCI}}{1.15}\right)^2 + (U_e)^2 + (\varepsilon_c)^2} \qquad\qquad (2.3.21)$$

# Chapter 3. Deterministic Simulation for Pipe Flow

## 3.1 Simulation domain and numerical scheme

Figure 3 shows a sketch of the computational domain and boundary conditions. The incompressible pipe flow was heated with uniform temperature at the pipe wall can be defined as below,

$$\theta = \frac{T_{wall} - T}{T_\tau} \tag{3.1.1}$$

where $T_{wall}$ is the average of temperature along the wall of the pipe, $T_\tau = \frac{q_{wall}}{\rho C_p u_\tau}$ is the frictional temperature with heat flux at the pipe wall $q_{wall}$, $u_\tau = \sqrt{\frac{\tau_{wall}}{\rho}}$ is the frictional velocity, with regard to shear stress on the wall $\tau_{wall} = \mu \frac{\Delta u}{\Delta x}$.
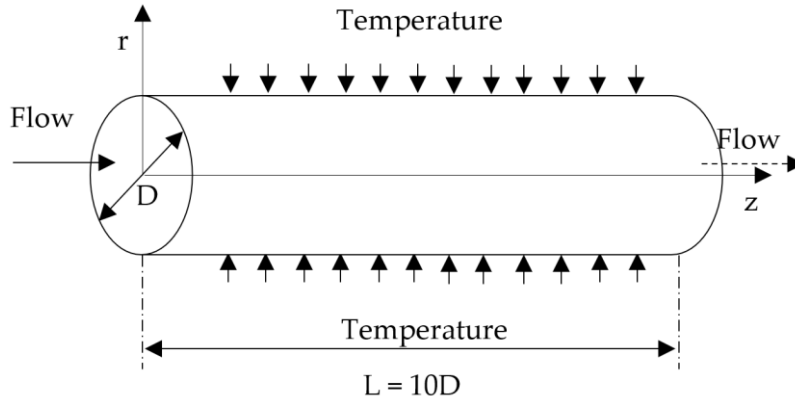


**Figure 3** *Schematic of the computational domain and the boundary conditions.*

The computational domain consists of a circular pipe of diameter $D$ and the pipe length in the streamwise direction, $L = 10D$. The effect of different orders of interpolated polynomials led to an increase in the number of grid points. The $P_N - P_N$ SEM formulation is considered for solution that mean the velocity space is approximated by typical $N^{th}$ order Lagrangian polynomial interpolations on the GLL points, and pressure space employs $N$ order of Lagrangian interpolants on the Gauss–Legendre quadrature points. The polynomial orders $N$ were set to 4, 6, and 8 on three different grid levels. The

accuracy of the solution with Reynolds number $Re = 19{,}000$ and Prandtl number $Pr = 0.71$ was examined according to three different grids. The time integration scheme uses the viscous terms treated implicitly by a third-order backward differentiation (BDF3), and the non-linear terms explicitly by a third-order extrapolation (EXT3) treatment, is BDF3/EXT3 scheme.

**Table 1** *Mesh characteristics.*

| Mesh levels | Spectral elements | Polynomial orders ($N$) | Number of nodes |
|:---:|:---:|:---:|:---:|
| Coarse | 1,120 | 4 | 71,680 |
| | | 6 | 241,920 |
| | | 8 | 573,440 |
| Medium | 4,800 | 4 | 307,200 |
| | | 6 | 1,036,800 |
| | | 8 | 2,457,600 |
| Fine | 15,360 | 4 | 983,040 |
| | | 6 | 3,317,760 |
| | | 8 | 7,864,320 |

Table 1 shows the details of the computational meshes of each case. Three grid levels were generated in coarse, medium, and fine mesh, with three different polynomial orders for each mesh. The nodes were distributed based on Gauss–Lobatto–Legendre points inside each spectral element. The GLL points distribution density of each element are based on number of orders of the elements. The high order elements will have more degree of freedom (Dof) due to the increased order. This is difference from increasing the refinement of the mesh by divide the computation domain more times to reduce element size. Thus, the total numbers of elements and nodes were promoted by increases of the polynomial order.

## 3.2 Statistical properties of velocity and temperature
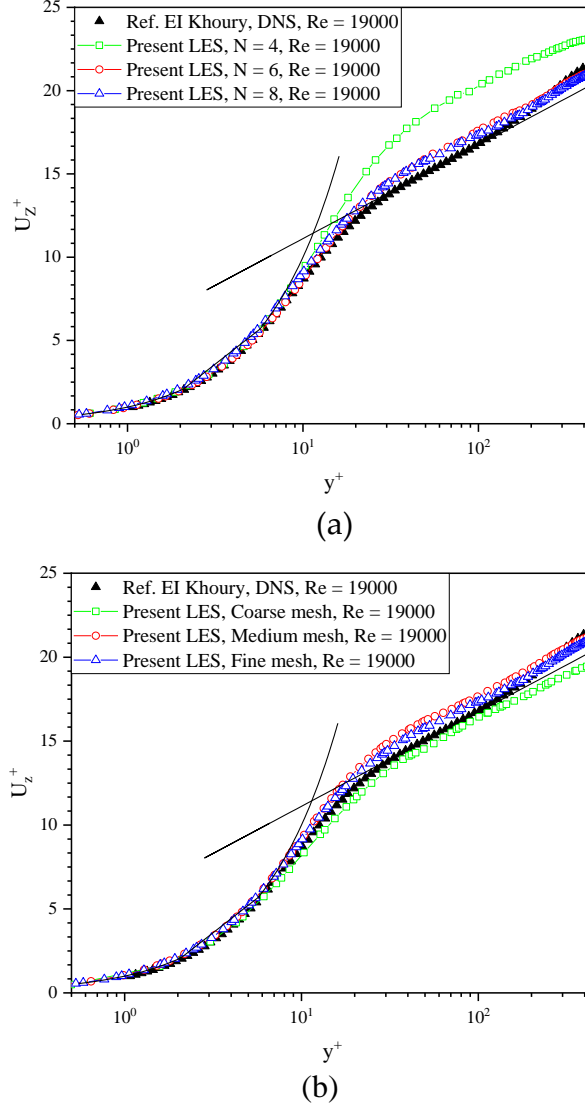
### 3.2.1 Mean velocity profile



(a)



(b)

**Figure 4** *Mean streamwise velocity profiles: (a) polynomial order effect, and (b) mesh effect.*

In Figure 4, the profiles of the mean streamwise velocities of the present simulation are compared with the DNS results by Khoury et al. (2013) [12] at the same Reynolds number and the law of the wall based on the wall unit $y^+$ (black line). In the viscous sublayer, the interval $0 \leq y^+ \leq 5$ is adhered to the linear law $U_z^+ = y^+$ and the interval $5 < y^+ \leq 30$ is the buffer region, while farther away from the wall, the interval $y^+ > 30$ follows the logarithm law as $U_z^+ = \frac{1}{k} ln(y^+) + \beta$ with the standard values of $k = 0.41$ and $\beta = 5.5$.

In Figure 4(a), the mean streamwise velocity profile is shown with the increasing polynomial orders (to the 4th, 6th, and 8th) which considered with fine mesh (15,360 spectral elements). The results of every order agree well with the DNS data and the law of the wall in the viscous sublayer region. However, the 4th order polynomial shows higher values than the results of the other orders and the reference data in the log law region the results, even though the finest mesh was employed. At the 6th and 8th polynomial orders the mean axial velocities $U_z^+$ are in good agreement with the DNS results of Khoury et al. (2013) [12].

The effect of the mesh type, coarse, medium, and fine, under the same polynomial order $N = 8$ are showen in Figure 4(b). Overall, the axial velocity profiles for the adopted three meshes agree well with the reference data [12] in all cases. This means that when the higher order of polynomial was adopted (in the current case, the 8th degree), the turbulent velocity profile in even the coarse mesh could be predicted well.

### 3.2.2 Root mean square velocity

Figure 5 and Figure 6 show the root mean square of the velocity fluctuations, $U_{\theta,rms}'^+$ in the azimuthal direction, $U_{r,rms}'^+$ in the axial, and $U_{z,rms}'^+$ in the radial, according to the different polynomial orders and the different grid levels. Figure 5 describes the root mean square of the velocity fluctuation of the 4th through 8th polynomial orders at the finest mesh. In the case of $U_{\theta,rms}'^+$ in the azimuthal direction, as the polynomial order increases at the fixed grid points the maximum value increase and the maximum value of RMS velocity moves around $y^+ = 15$.
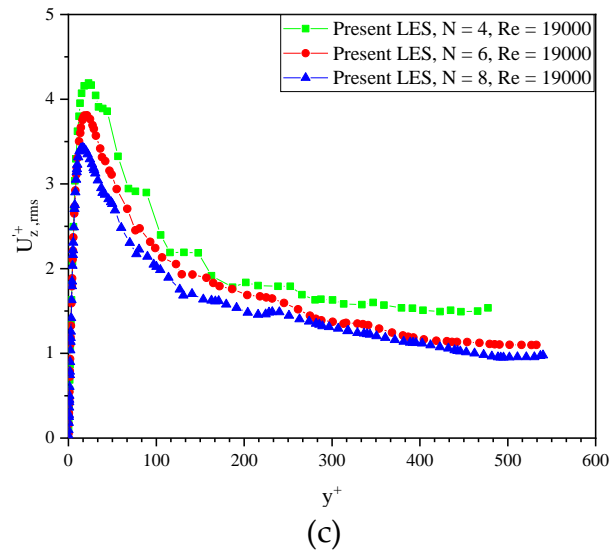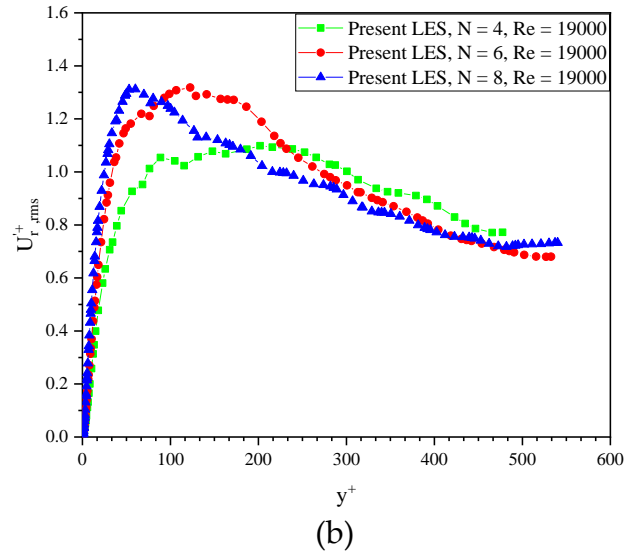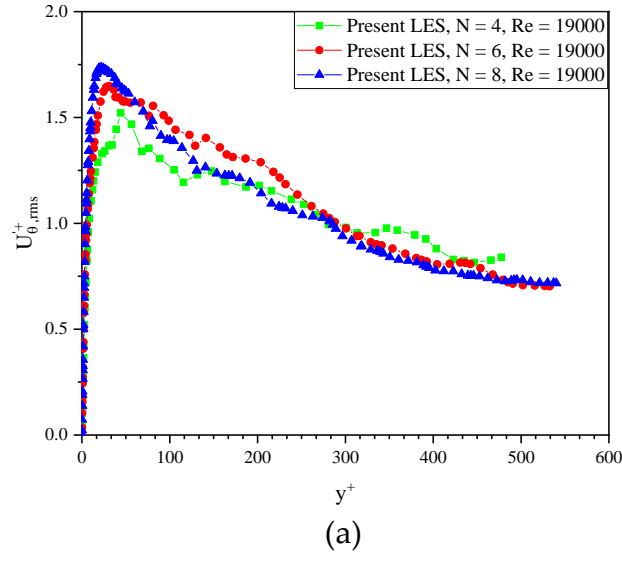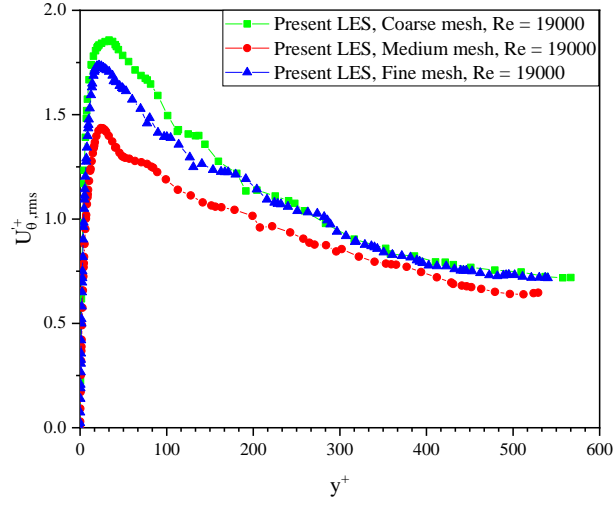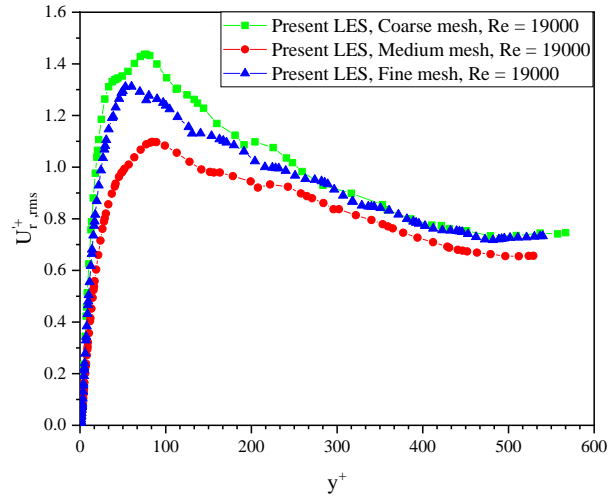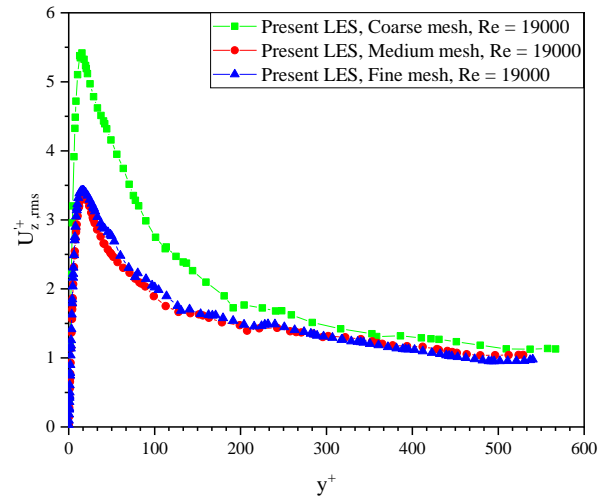
**Figure 5** *RMS velocity as related to the polynomial order: (a) azimuthal, $U_{\theta,rms}^{+}$; (b) axial, $U_{r,rms}^{+}$; (c) radial $U_{z,rms}^{+}$.*

31

(a)



(b)



(c)

**Figure 6** *RMS velocity as related to the grid level: (a) azimuthal, $U^+_{\theta,rms}$; (b) axial, $U^+_{r,rms}$; (c) radial $U^+_{z,rms}$.*

However, at the fixed polynomial order $N = 8$, the peak decreases with the increasing number of grid points (Figure 6(a)). Similar behavior can be seen in $U'^+_{r,rms}$ in the axial direction in Figure 5(b) and Figure 6(b). In the radial direction, $U'^+_{z,rms}$, as the polynomial order increases or the number of grid points increases, the peak value decreases. However, the location of the maximum value is predicted to be around $y^+ = 15$ in all cases. This demonstrates that the velocity fluctuation in every direction is more sensitive to the polynomial order than to grid level.

### 3.2.3 Mean temperature profile

The mean temperature distribution versus the distance in the wall unit, $y^+$ with the different polynomial orders and grid levels are showed in Figure 7 which are compared with the LES computation by Ould-Rouiss, Bousbai, and Mazouz (2013) [8], Their simulation is considered heat transfer pipe flow at the Prandtl number $Pr = 0.71$ and the Reynolds number $Re = 20,000$, and the uniform heat flux was applied to the wall instead of the uniform temperature in the present simulation.

Similar to the comparison of mean axial velocity profiles above, the mean temperature profiles in cases of the 6th and 8th polynomial orders agree fairly well with the reference value (Ould-Rouiss, Bousbai, and Mazouz, 2013) [8], as shown in Figure 7(a). However, the predicted profile in the 4th order case shows a large discrepancy from the reference. These correspond to the result in the fine mesh.

In the case of the 8th polynomial order (Figure 7(b)), the predicted mean temperature profile does not depend on the grid level, and all the predicted values are consistent with each other and the reference data (Ould – Rouiss, Bousbai, and Mazouz 2013) [8].
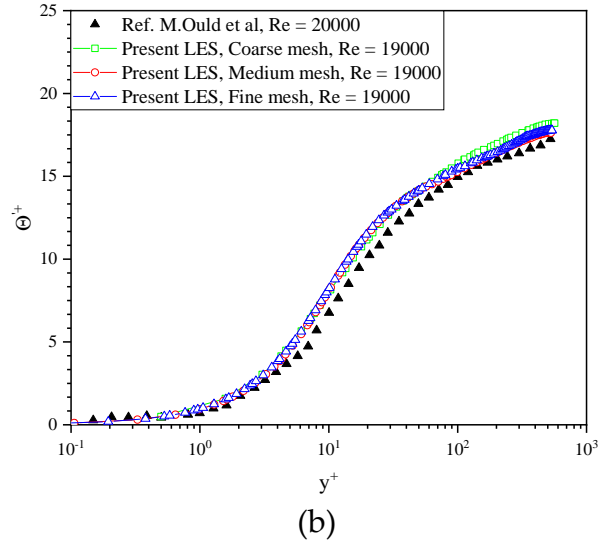
(a)



(b)
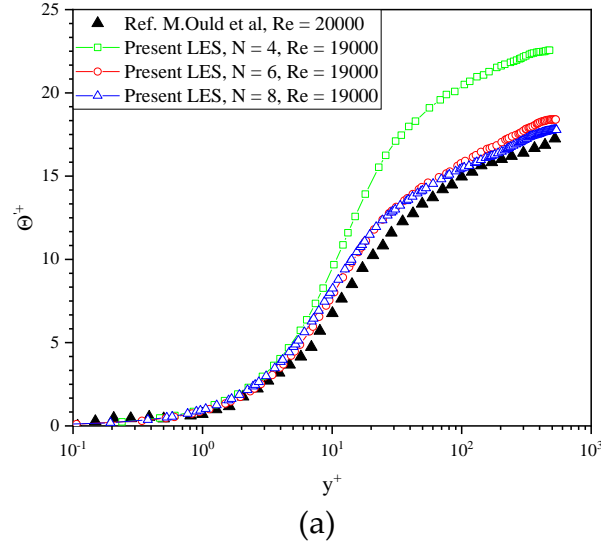
**Figure 7** *Mean temperature profiles: (a) polynomial order effect, and (b) mesh effect.*

### 3.2.4 Heat flux

In Figure 8 shows the streamwise/axial turbulent heat flux as a function of the distance from the wall $y^+$, at various polynomial orders (Figure 8(a)) and grid levels (Figure 8(b)). Our simulation results are compared with the LES results from Ould – Rouiss, Bousbai, and Mazouz (2013) [8], with different wall conditions (the uniform heat flux was applied to the wall instead of the uniform temperature in the present simulation) and small differences in the Reynolds number, $Re = 20,000$ (the Reynolds number in present work is $Re = 19,000$). We wanted to compare only the behavior of the heat flux with increases

in the wall distance. The turbulent heat flux increased as the distance to the wall increased, with a peak at approximately $y^+\sim10$, and then decreased to zero.



(a)



(b)
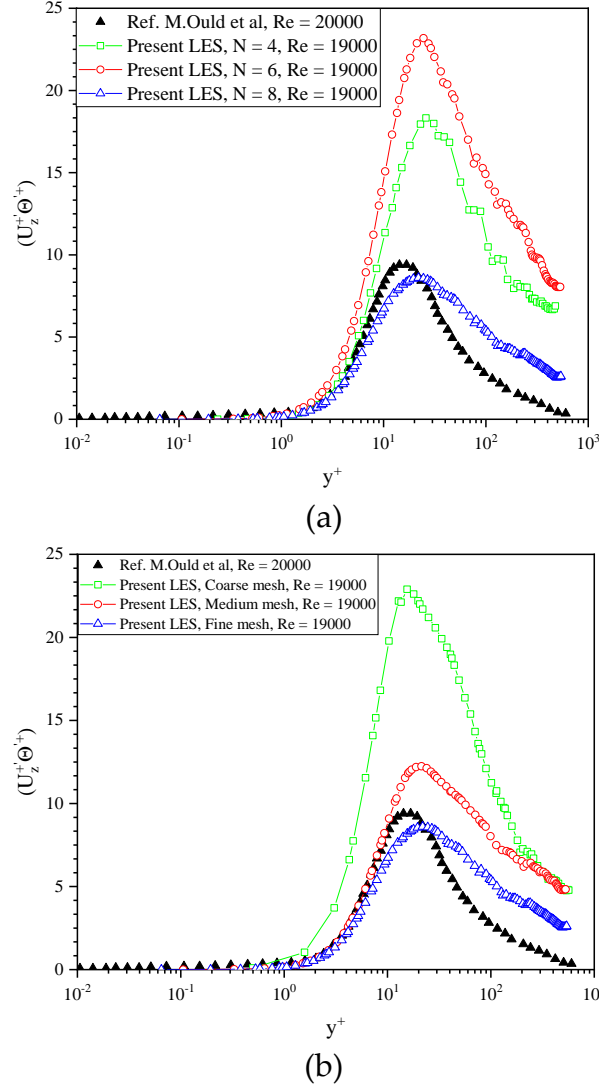
**Figure 8** *Streamwise turbulent heat flux: (a) polynomial order effect, and (b) mesh effect.*

In the difference of polynomial order cases (Figure 8(a)), the profile of the turbulent heat flux in the streamwise direction approached the values of the LES results by Ould – Rouiss, Bousbai, and Mazouz (2013) [8], However, the position of the maximum turbulent heat flux was located at approximately $y^+\sim 20$ instead of $y^+\sim 10$ in the LES results. This discrepancy was caused by the different boundary conditions at the wall.

The effect of grid level within one interpolation polynomial order, $N = 8$, is showed

in Figure 8(b). The mesh is finer, and the agreement with the profile from LES Ould – Rouiss, Bousbai, and Mazouz (2013) [8] is better. Although the higher-order polynomial (up to 8th degree) was used, the coarse mesh in our present work was not enough to resolve the turbulent heat flux. The interesting point is that all the cases with different grid levels predicted the peak of the heat flux near the same position, at $y^+ \sim 20$.

### 3.2.5 Instantaneous flow fields

Figure 9 shows the contours of the instantaneous axial velocity at the cross section ($x/D = 5.0$) of the computational domain in Figure 3. The contours in Figures 9(a), (b), and (c) correspond to the same number of spectral elements, 15,360, which is the fine mesh case with three different polynomial orders, the 4th, 6th, and 8th. In the results, the total numbers of nodes are 983,040 in 4th order case, 3,317,760 in the 6th, and 7,864,320 in the 8th. As the polynomial order increased, the flow fields were able to be resolved with smaller eddies, especially near the wall. However, when the polynomial order was low, it can be seen that only large eddies were resolved.

The effect of the grid number is presented in Figures 9(c), (d), and (e), where the total spectral elements for each case are 1,120, 4,800, and 15,360, respectively. The polynomial order is fixed as $N = 8$ in this figure. More small eddies near the wall can be observed in the fine mesh. However, the resolution difference between the coarse and fine meshes is not more severe than that between the low and higher polynomial orders shown in Figures 9(a), (b) and (c). This result can be confirmed by the predictions of mean velocity and temperature in Figures 4 and 7.

The instantaneous temperature fields in the pipe at the center cross section of the computational domain (Figure 3) for the different polynomial orders are shown in Figure 10(a), (b), and (c). The thermal structures exist in the whole pipe section and extend from the pipe center to the wall. The molecular heat flux is reduced when the polynomial order

is reduced. As the polynomial order is increased, the wall normal turbulent heat flux is intensified. The motion near the wall is more resolved in the higher-order polynomials.

The effect of the grid number on the instantaneous temperature field is shown in Figure 10(c), (d), and (e). The normal wall turbulent heat flux is enhanced when a finer grid is used. However, the difference between the coarse mesh and the fine mesh is insignificant compared with that between the low and higher polynomial orders.
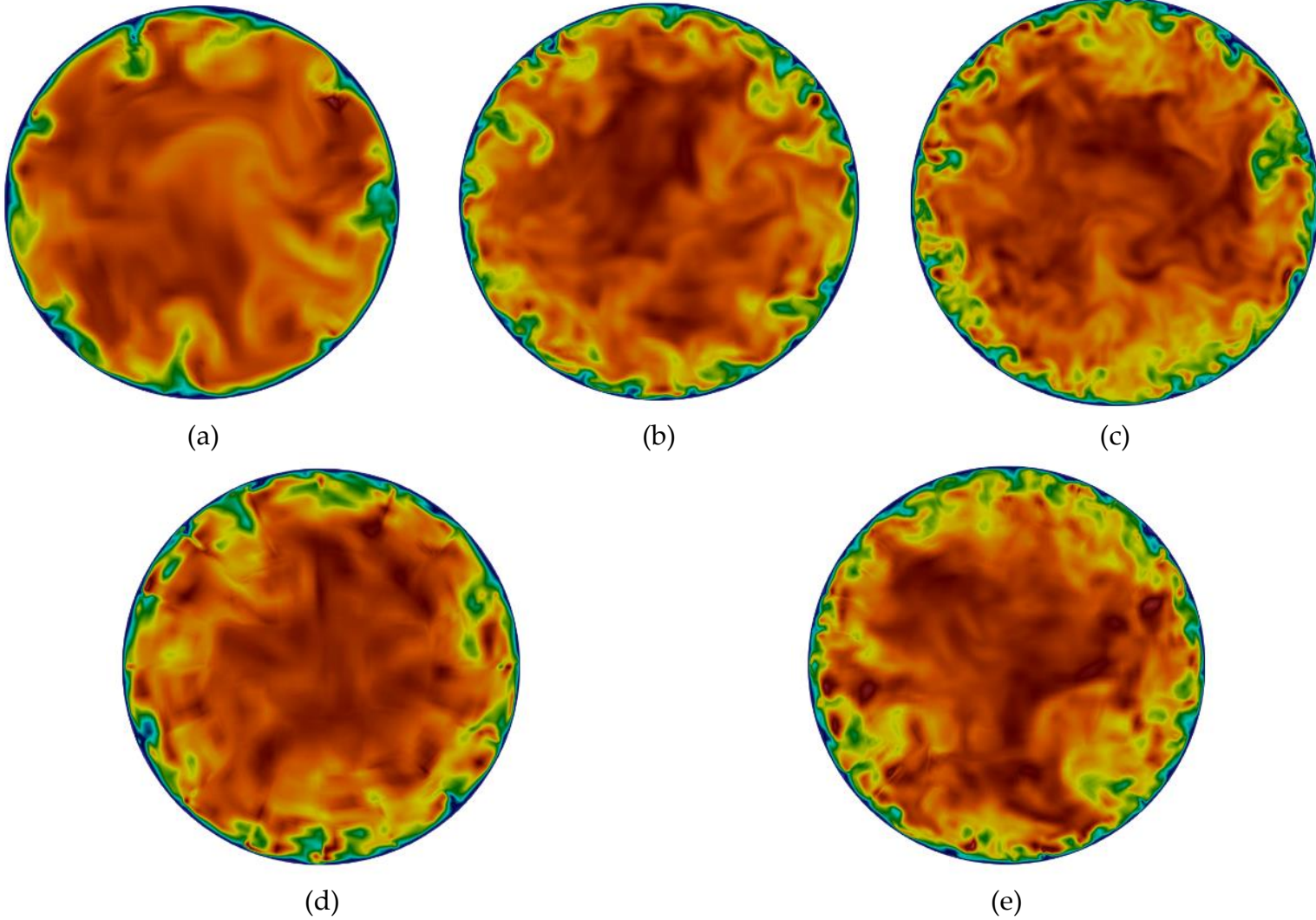
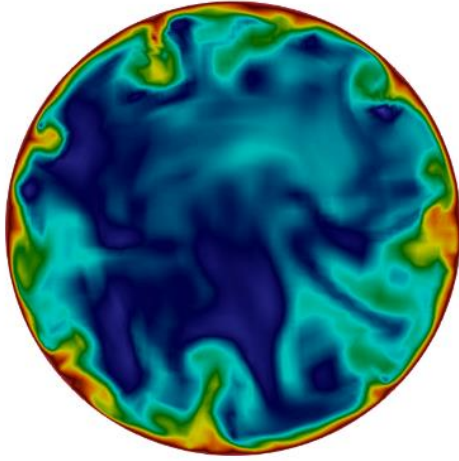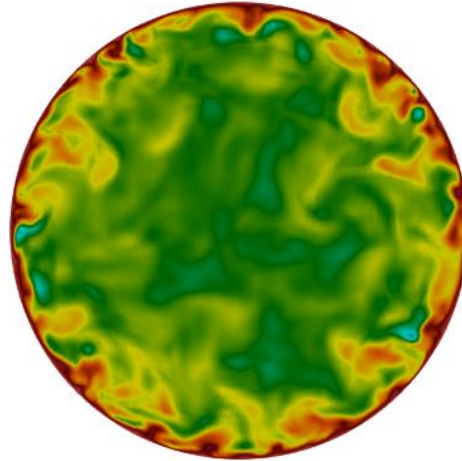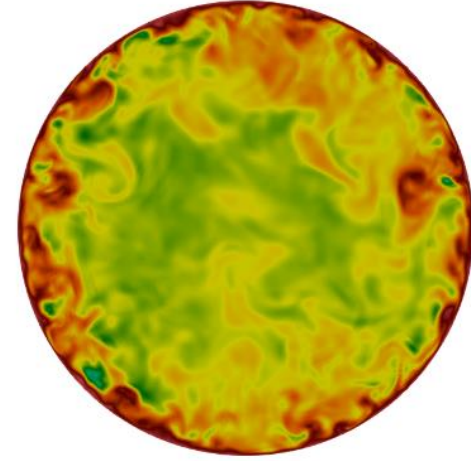**Figure 9** *Contours of the instantaneous axial velocity: (a) fine mesh with N = 4; (b) fine mesh with N = 6; (c) fine mesh with N = 8; (d) coarse mesh with N = 8; (e) medium mesh with N = 8.*

**Figure 10** *Contours of the instantaneous temperature: (a) fine mesh with N = 4; (b) fine mesh with N = 6; (c) fine mesh with N = 8; (d) coarse mesh with N = 8; (e) medium mesh with N = 8.*

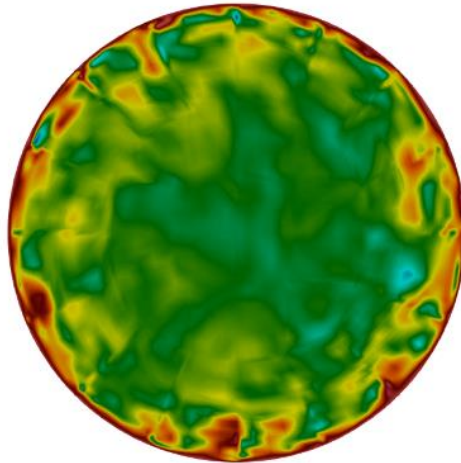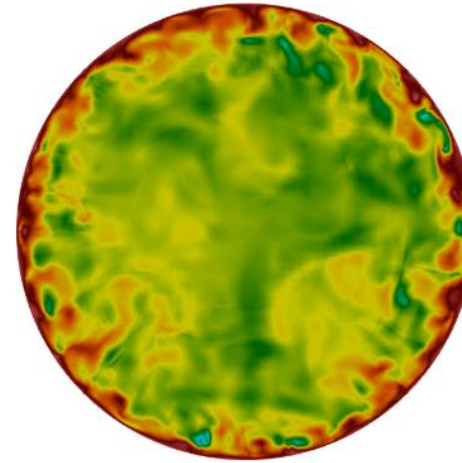### 3.2.6 Computing memory and runtime

In analysis and design processes based on CFD, the computational time is equally as important as the accuracy of the solution. This section provides detailed information pertaining to computational efficiency, including running time and memory used. Table 2 presents the information of all the cases according to the mesh number and polynomial order. All simulations were carried out on a high-performance computing system with an Intel® Xeon® E5-2690 processor.

**Table 2** *Run time and computer memory.*

| Mesh levels | Polynomial orders (N) | Total time (minutes) | Time/one step (second) | Memory used (GB) |
|---|---|---|---|---|
| Coarse | 4 | 5.754 | 0.081 | 2.57311 |
| | 6 | 26.223 | 0.232 | 6.00920 |
| | 8 | 116.686 | 0.467 | 8.44489 |
| Medium | 4 | 30.636 | 0.505 | 2.72006 |
| | 6 | 298.838 | 1.517 | 9.95910 |
| | 8 | 2,027.100 | 4.422 | 15.7682 |
| Fine | 4 | 167.650 | 1.810 | 5.46292 |
| | 6 | 2,081.333 | 6.836 | 11.4328 |
| | 8 | 13,354.100 | 21.348 | 22.0713 |

Considering the size of the mesh and the polynomial order is important for optimal computation time and memory capacity while still ensuring the accuracy of the results. In the fine mesh case with the polynomial order of 8, 15,360 spectral elements were used, and the total grid points were 7,864,320. The total run time in this case was up to 13,354 minutes and required more than 22 GB of memory.

The total runtime and required memory capacity based on the 6th order polynomial are much less than those of the 8th order polynomial in the same mesh. The total runtime based on the 6th order polynomial is four times less than in coarse mesh, six times in medium mesh and fine mesh. Moreover, nearly two times less for memory capacity when the 6th-

order polynomial is applied, while the difference of the 6th and 8th order polynomial results are insignificant. In the comparison to difference mesh (coarse, medium, and fine mesh) with the same order of polynomial ($N = 8$), there is no difference between the results of medium and fine mesh (see in sections 3.2.1, 3.2.2 and 3.2.3), although the total runtime in medium mesh is only 2,027 minutes which is six times less than that in fine mesh and the memory capacity can be saved nearly two times.

## 3.3 Grid convergence index

In this section, two GCI estimations are investigated to the grid and polynomial order in the adopted SEM. The Nusselt number, which is typically a dimensionless parameter in the heat transfer of a pipe, was selected as the quantity of interest (QoI) in the present study. The mathematical formula of the Nusselt number based on the bulk temperature can be expressed as follows:

$$Nu = \frac{hD}{k} = \frac{2q_w r_w}{k\left(T|_{r=r_w} - T_b\right)} \tag{3.3.1}$$

where the mass average (bulk) temperature, $T_b$, is defined as follows by averaging the velocity profile $\tilde{u}(r)$ and the temperature $\tilde{T}(x, r)$ in time,

$$T_b(x) = \frac{2}{r_w^2 u_{mean}} \int_0^{r_w} \tilde{u}(r) \, \tilde{T}(x, r) r dr \tag{3.3.2}$$

To calculate the GCI value, three different grids (coarse, medium, and fine) at one fixed order, $N = 8$, and three different polynomial orders ($N = 4, 6,$ and 8) at the fine mesh were considered. Figures 11(a), (b), and (c) show the fine mesh at the cross section with 4th, 6th, and 8th order polynomials. Figures 11(d) and (e) correspond to the coarse and medium mesh, respectively, at the fixed polynomial order, $N = 8$, with 8 GLL points at each element. These study parameters are summarized in Table 3 and Table 4 for polynomial orders effect and mesh levels effect, respectively.

41

Among the three available GCI estimation methods (the original Roache's method, Mod. – ASME, and SLS – GCI), we used the latter two in the present study since the original Roache's method requires a monotonic solution (increasing or decreasing results simultaneously between different grid systems). However, the present results do not show this behavior, which is typical in most engineering simulations.

**Table 3** *Characteristics of polynomial orders effective with number of spectral elements,* 15,360.

| Polynomial orders ($N$) | Number of elements | f-value (Nusselt number) |
|---|---|---|
| 4 | 414,720 | 50.564 |
| 6 | 1,920,000 | 49.803 |
| 8 | 5,268,480 | 49.947 |

**Table 4** *Characteristics of mesh levels effective with polynomial order, $N = 8$.*

| Mesh levels | Number of elements | f-value (Nusselt number) |
|---|---|---|
| Coarse | 382,160 | 49.901 |
| Medium | 1,646,400 | 49.324 |
| Fine | 5,268,480 | 49.947 |

In the GCI estimation, the is reference solution of the Nusselt number is necessary considered, here as the correlation proposed by Gnielinski [21]. This correlation can be calculated using the friction coefficient correlation, the Prandtl number, and the Reynolds number as follows:

$$Nu = \frac{(f/8)(Re - 1000)Pr}{1 + 12.7(f/8)^{1/2}(Pr^{2/3} - 1)} \tag{3.3.3}$$

where the friction coefficient correlation is given by

$$f = (0.79ln(Re) - 1.64)^{-2} \tag{3.3.4}$$

The Gnielinski correlation is valid for $0.5 \leq Pr \leq 2,000$ and $3 \times 10^3 \leq Re \leq 5 \times 10^6$.
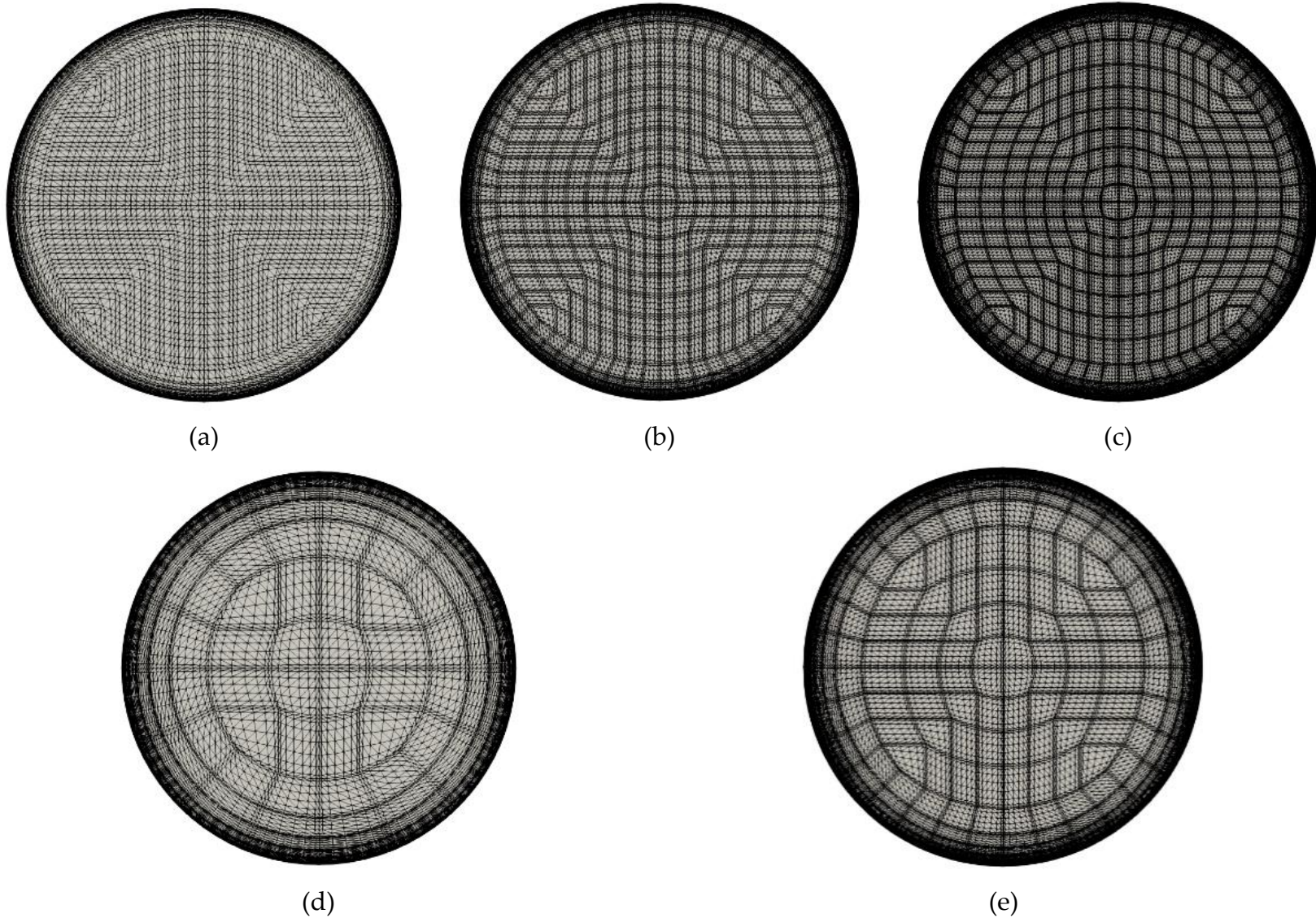
(a)

(b)

(c)

(d)

(e)

**Figure 11** *Mesh arrangements: (a) fine mesh with $N = 4$; (b) fine mesh with $N = 6$; (c) fine mesh with $N = 8$; (d) coarse mesh with $N = 8$; (d) medium mesh with $N = 8$.*

In this simulation, the computed Nusselt number by the Gnielinski correlation [21] is $Nu = 49.753$ when the Reynolds number $Re = 19,000$ and the Prandtl number $Pr = 0.71$ as the reference result.

**Table 5** *GCI estimation.*

| Effects | Mod. – ASME | | | SLS – GCI | | | |
|---|---|---|---|---|---|---|---|
| | $u_{GCI}$ | $f_c$ | $\varepsilon$ (%) | $u_{GCI}$ | $u_e$ | $f_c$ | $\varepsilon$ (%) |
| Polynomial orders | 0.2486 | 50.030 | 0.5562 | 0.0635 | 0.3867 | 49.865 | 0.2248 |
| Mesh levels | 0.8489 | 50.230 | 0.9584 | 0.0179 | 0.1182 | 49.636 | 0.2365 |

The results of our two GCI estimations by the Mod. – ASME and the SLS–GCI methods are summarized in table 5. The extrapolation value from the SLS–GCI method seemed to be better in terms of difference from the reference solution: $\varepsilon = 0.2248\%$ for the polynomial order effect case and $\varepsilon = 0.2365\%$ for the mesh number effect case. In the Mod. – ASME method, the difference from the reference solution, $\varepsilon$, are more than two times larger than those of the SLS – GCI, as listed in Table 5. The GCI values, $u_{GCI}$, by SLS–GCI are 0.0635 and 0.0179 for the polynomial order and the mesh cases, respectively, while the Mod. – ASME method predicted these up to 0.2486 and 0.8489 for the two effect cases. The GCI value from the Mod. – ASME method was estimated based on the difference between the extrapolated value and the numerical value at the fine mesh, while the SLS – GCI method estimated the GCI value through the difference between the two values by a power law. Thus, the Mod. – ASME's insufficient results of the GCI value was due to its poor extrapolation compared with the SLS – GCI, although the difference between the Mod. – ASME's extrapolation results and the exact results was not bad.

# Chapter 4. Deterministic Simulation for Rod Bundle flow

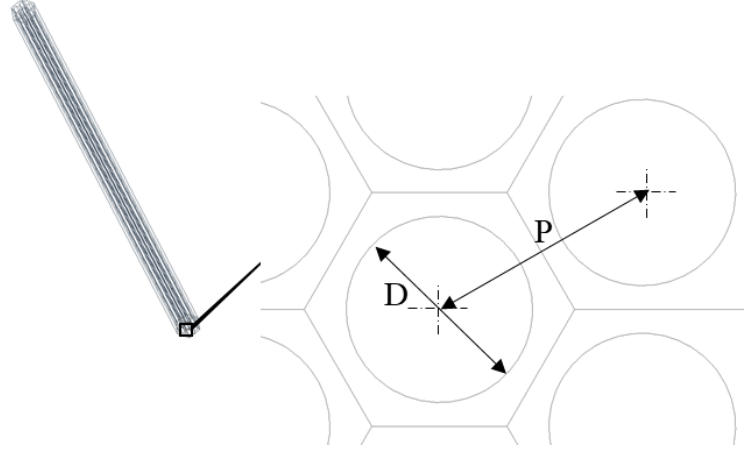## 4.1 Computational domain and numerical scheme



**Figure 12** *Geometry for bare rod.*

The bare rod is hexagonal rods that are close together, thus, there is symmetry between the rods (figure 12). We are able to be take the advantage of the symmetries of the flow to solve single rod instead of the full domains.



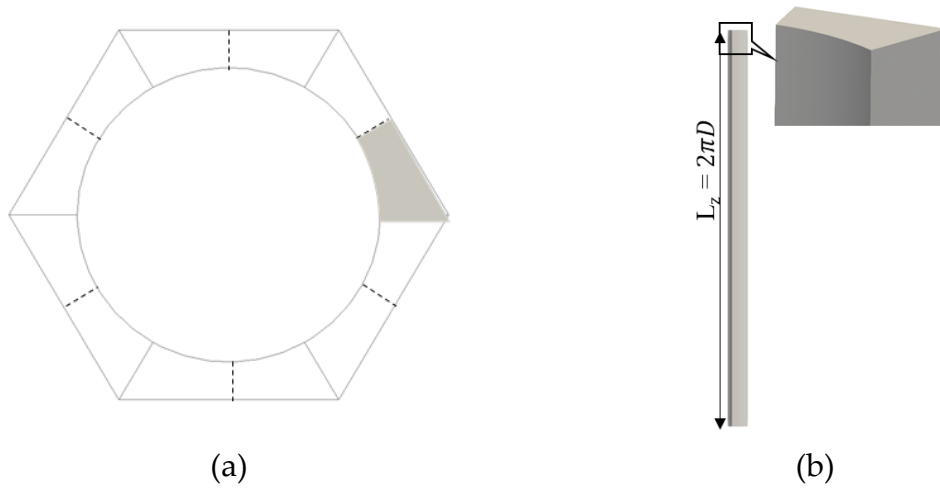(a)                                                    (b)

**Figure 13** *(a) Geometry for single rod; (b) Geometry definition for LES presentation.*

In this simulation, the single rod is considered with *P/D* of 1.24. To reduce computational cost, one may take advantage of the symmetries of the domain. In single rod able to be divided into twelve homologous sections as figure 13(a). Figure 13(b) show

the geometry employed for the different simulation performed with the length of domain is $L_z = 2\pi D$. The simulation has been performed under incompressible conditions and in their dimensionless form. The Reynold number based on those is $Re = 10,000$ and the Prandtl number of the fluid is a constant $Pr = 1.0$. The energy equation has been solved in its dimensionless form as,

$$T^* = \frac{T - T_0}{\Delta T} \tag{4.1.1}$$

where $T_0$ s the uniform temperature at the inlet.



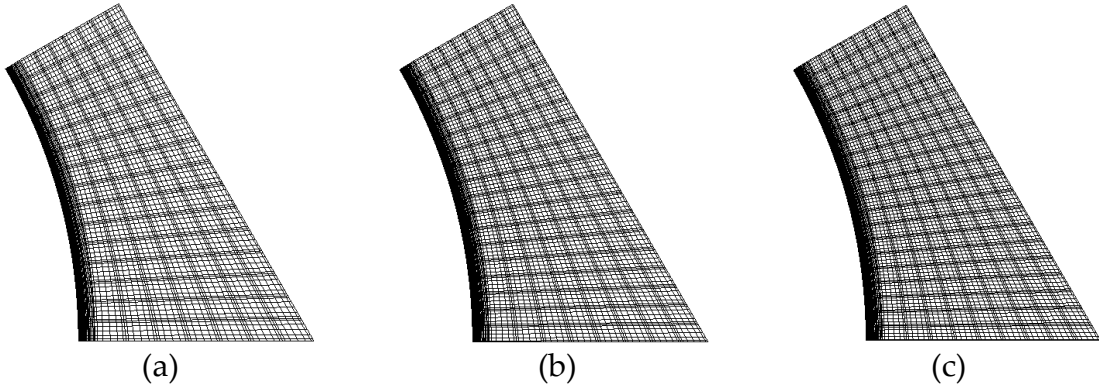<div align="center">(a)         (b)         (c)</div>

**Figure 14** *Mesh arrangement with polynomial order of 7: (a) coarse mesh; (b) medium mesh; (c) fine mesh.*

The $P_N - P_{N-2}$ SEM formulation is considered for solution with $N = 7$ that mean the velocity space is approximated by typical 7th order Lagrangian polynomial interpolations on the GLL points, and pressure space employs 5th order of Lagrangian interpolants on the Gauss–Legendre quadrature points. The time integration scheme with the viscous terms treated implicitly by a second – order backward differentiation (BDF2), and the non-linear terms explicitly by a second – order extrapolation (EXT2) treatment, is BDF2/ EXT2 one.

Structured meshes have been considered for three different grid levels (coarse, medium, and fine) at the fixed order of 7th order, which is showed in figure 14. Table 6 shows the details of the computational meshes of coarse, medium, and fine mesh case. The

Gauss – Lobatto – Legendre points distribution, leading to total number of grid points $n = EN^3$.

**Table 6** *Mesh arrangement for the fixed order, $N = 7$.*

| Case | Spectral element |
|------|------------------|
| Coarse | 12,600 |
| Medium | 21,870 |
| Fine | 29,760 |

## 4.2 Evaluation results of velocity and temperature
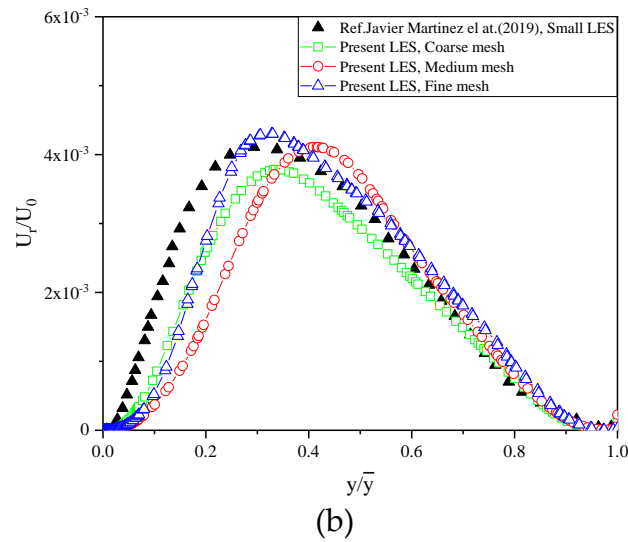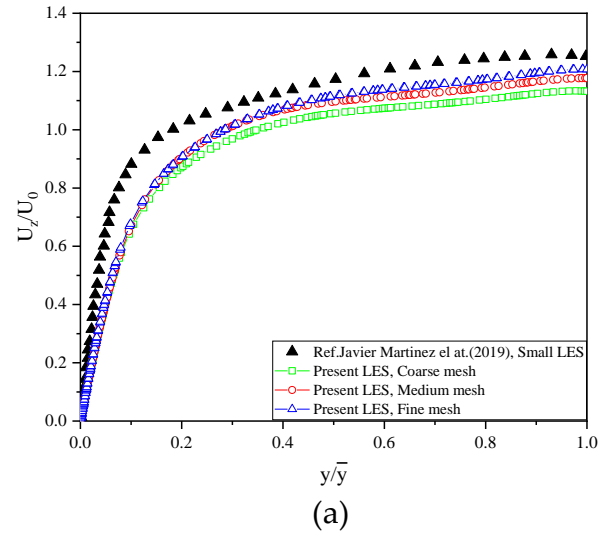
### 4.2.1 Velocity profile



(a)



(b)

**Figure 15** *Velocity profile: (a) Axial velocity, and (b) Radial velocity.*

In Figure 15, the profiles of the axial velocity (figure 15(a)) and radial velocity (figure 15(b)) of the present simulation are compared with the single rod bundle results by Javier Martínez et al. (2019) [16] at the same Reynolds number. The axial velocity profiles approached the values of the single rod LES results by Javier Martínez et al. (2019) [16]. In radial velocity (figure 15(b)), the profile with mesh finer is agreement with that from reference results (Javier Martínez et al. (2019) [16]).

### 4.2.2 Instantaneous flow fields



| (a) | (b) | (c) |
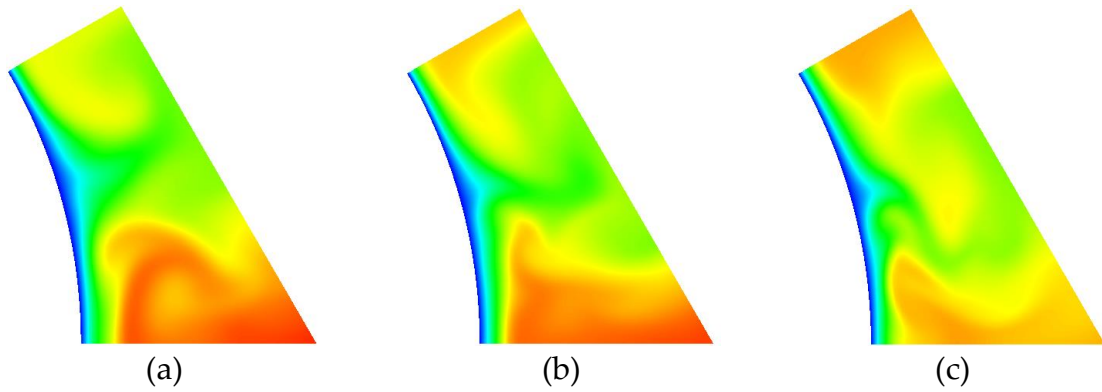
**Figure 16** *Contours of the instantaneous axial velocity: (a) coarse mesh; (b) medium mesh; (c) fine mesh.*

Figures 16 (a), (b), and (c) show the contour of the instantaneous axial velocity, where the total spectral elements for each case are 12,600, 21,870, and 29,760, respectively. The polynomial order is fixed as $N = 7$ in this figure. This shows that the resolution of fine mesh is higher than that of coarse mesh.

### 4.3 Grid convergence index

Though GCI estimation according to the polynomial order and grid levels in the pipe simulation results, it was found that the accuracy of the SLS – GCI method is greater than that by Mod. – ASME. Thus, the SLS – GCI method is chosen to study uncertainty quantification by GCI estimation for rod – bundle results effect of grid level.
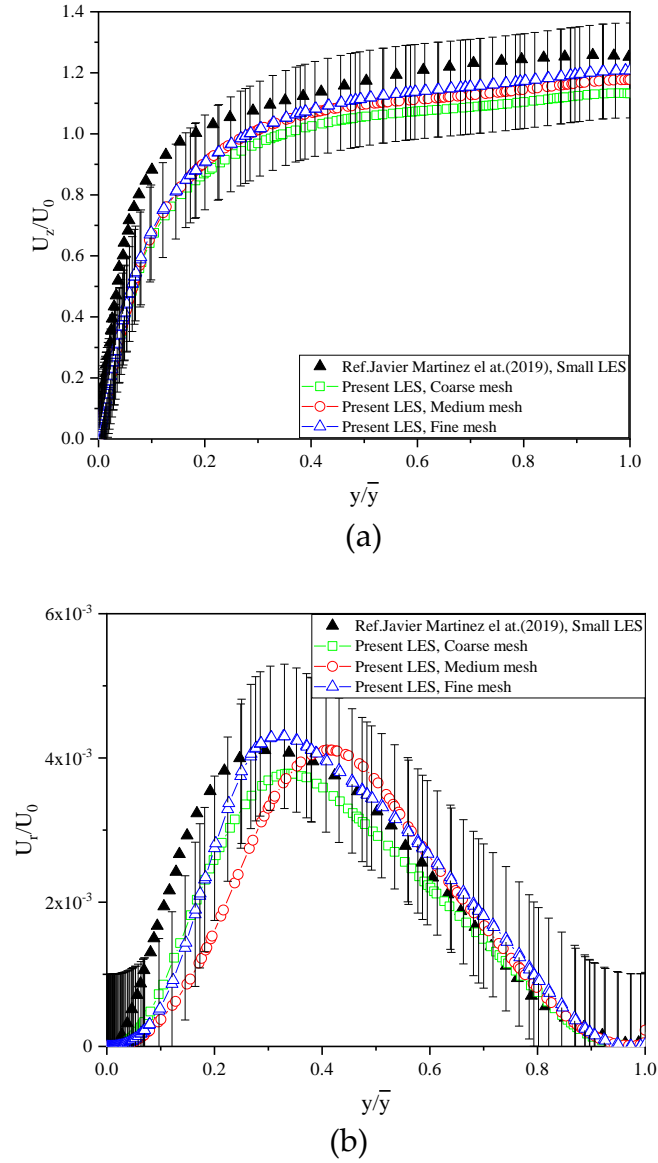
**Figure 17** *Velocity profile of time averaged: (a) Axial velocity; (b) Radial velocity. The error bars on the numerical results of the combined standard uncertainties $U_S$.*

Specifications of the mesh arrangement for GCI estimation are listed in table 5 (in section 4.1). The total number of elements in the mesh arrangement of coarse, medium, and fine meshes are 2,721,600, 4,723,920, and 6,428,160, respectively. The simulation results for axial/radial velocity are performed in section 4.2 to provide the data for GCI estimation. Table 5 summarizes the estimation results of the uncertainty quantification by the SLS – GCI. The error of exact and numerical results $\varepsilon_0$ in axial and radial velocity are 13.24% and 6.38%, respectively, as listed in table 7. The combined standard uncertainty

$U_S$ of 16.46% and 8.47% of axial velocity and radial velocity are showed by the error bar on the numerical results, respectively, as showed by the error bar on the numerical results in Figure 16. The error of exact and numerical results $\varepsilon_0$ is smaller than that of uncertainty value $U_S$.

**Table 7** *Summarizes the results of SLS – GCI estimation.*

| Case | $\varepsilon_0$ | SLS - GCI | | | |
| --- | --- | --- | --- | --- | --- |
| | | $U_{GCI}$ | $U_e$ | $\varepsilon_c$ | $U_S$ |
| $U_z/U_0$ | 0.1324 | 0.1009 | 0.0593 | 0.1209 | 0.1554 |
| $U_r/U_0$ | 0.0638 | 0.0538 | 0.0301 | 0.0830 | 0.1000 |

Where the index of $\varepsilon_0$ in table 6 is the error between the reference results and the numerical result in case – F, $f_1$. The index of $\varepsilon_0$ estimated is estimated as follows:

$$\varepsilon_0 = \sqrt{\frac{1}{M}\sum_{j=1}^{M}\{|(f_0)_j - (f_1)_j|\}^2} \qquad (4.3.1)$$

# Chapter 5. Conclusion

## 5.1 Conclusion

Large eddy simulation of turbulent heat transfer flows (with two geometries, pipe flow and rod bundle flow) were conducted using NEK5000 code based on the spectral element method and two GCI estimation methods were used here, the modified Roache's method introduced in the ASME V&V 20-2009 guideline (Mod. – ASME) and Eca's least square version (SLS–GCI).

In pipe flow simulation, the diameter of the pipe was D, and the axial extent of the domain was $10D$ at Reynolds number $Re = 19,000$ and Prandtl number $Pr = 0.71$. The objective of the present research was to observe the interpolation effects of different polynomial orders and grid sizes on SEM-based simulation results. The polynomial order ranged from 4th to 8th, and three grids (coarse, medium, and fine) were considered. The statistical quantities, including the mean velocity, the RMS of the velocity fluctuations, the mean temperature, and the axial heat flux, were examined, and the results were in good agreement with the reference results at higher-order polynomials. The effect of grid size at the higher-order polynomials was less than the effect of the polynomial order at the fixed mesh size. This means that even coarse mesh was able to resolve the small turbulent eddies near the wall if a higher-order polynomial was adopted. However, if the polynomial order was low, the fine mesh was not able to capture the flow and temperature features correctly.

The modified Roache's method introduced in the ASME V&V 20-2009 guideline (Mod. – ASME) and Eca's least square version (SLS–GCI), along with three mesh arrangements (coarse, medium, and fine) and three difference polynomial order (4th, 6th, and 8th). The error index from the SLS–GCI estimation was two times less than that of the Mod. – ASME estimation. Further, GCI was estimated as being smaller by SLS–GCI than

by Mod. – ASME.

Though GCI estimation of polynomial order and grid levels effect case in the pipe results, it was found that the accuracy of the SLS – GCI method is greater than that by Mod. – ASME. Thus, the SLS – GCI has been chosen to study uncertainty quantification by GCI estimation for rod – bundle results effect of grid level in rod bundle simulation. The error of exact and numerical results is smaller than that of uncertainty value.

## 5.2 Future work

The turbulent kinetic energy of the rod bundle simulation will be investigated. The thermal field for rod – bundle simulation will be studied and the GCI estimation for the numerical results will be conducted.

In the future, uncertainty quantification with the spectral element method will be investigated in the influence of other input parameters on the numerical solution, the computing time, and the number of solver iterations, for instance.

# REFERENCES

1. Roache, P.J., *Verification and validation in computational science and engineering*. 1998, Albuquerque, N.M.: Hermosa Publishers. xvi, 446 p.

2. Richardson, L.F. and J.A. Gaunt, *VIII. The deferred approach to the limit.* Philosophical Transactions of the Royal Society of London. Series A, Containing Papers of a Mathematical or Physical Character, 1927. **226**(636-646): p. 299-361.

3. Richardson, L.F. and R.T. Glazebrook, *On the approximate arithmetical solution by finite differences of physical problems involving differential equations, with an application to the stresses in a masonry dam.* Proceedings of the Royal Society of London. Series A, Containing Papers of a Mathematical and Physical Character, 1910. **83**(563): p. 335-336.

4. Coleman, H. and C. Members, *Standard for Verification and Validation in Computational Fluid Dynamics and Heat Transfer (V&V20 Committee Chair and principal author).* ASME V&V 20-2009, 2009.

5. Tanaka, M. and Y. Miyake, *Numerical simulation of thermal striping phenomena in a T-junction piping system for fundamental validation and uncertainty quantification by GCI estimation.* Mechanical Engineering Journal, 2015. **2**(5): p. 15-00134-15-00134.

6. Eça, L. and M. Hoekstra, *Discretization Uncertainty Estimation Based on a Least Squares Version of the Grid Convergence Index.* Proceedings of the 2nd Workshop on CFD Uncertainty Analysis, 2006.

7. Tavakoli, E., Hosseini, R., Papalexandris , M., Lessani, B., *Statistical analysis of instantaneous turbulent heat transfer in circular pipe flows.* Heat and Mass Transfer, 2014. **50**(1): p. 125-137.

8. Ould-Rouiss, M., M. Bousbai, and A. Mazouz, *Large eddy simulation of turbulent heat transfer in pipe flows with respect to Reynolds and Prandtl number effects.* Acta Mechanica, 2013. **224**(5): p. 1133-1155.

9. Abe , H., H. Kawamura, and Y. Matsuo, *Direct Numerical Simulation of a Fully Developed Turbulent Channel Flow With Respect to the Reynolds Number Dependence.* Journal of Fluids Engineering, 2001. **123**(2): p. 382-393.

10. Patera, A.T., *A spectral element method for fluid dynamics: Laminar flow in a channel expansion.* Journal of Computational Physics, 1984. **54**(3): p. 468-488.

11. Fischer, P., Kerkemeier, S., Peplinski, A., Shaver, D., Tomboulides, A., Min, M., Obabko, A., Merzari, E., *nek5000 web page*. 2008; Available: http://nek5000.mcs.anl.gov.

12. El Khoury, G., Schlatter, P., Noorani, A., Fischer, P., Brethouwer, G., Johansson, A., *Direct Numerical Simulation of Turbulent Pipe Flow at Moderately High Reynolds Numbers.* Flow, Turbulence and Combustion, 2013. **91**(3): p. 475-495.

13. Antoranz, A., Gonzalo, A., Flores, O., García-Villalba, M., *Numerical simulation of heat transfer in a pipe with non-homogeneous thermal boundary conditions.* International Journal of Heat and Fluid Flow, 2015. **55**: p. 45-51.

14. Ryzhenkov, V., Ivashchenko, V., Vinuesa, R., Mullyadzhanov, R., *Simulation of heat and mass transfer in turbulent channel flow using the spectral-element method: Effect of spatial resolution*. Journal of Physics: Conference Series (JPCS), 2016.

15. Wang, Z., Örlü, R., Schlatter, P., Chung, Y., *Direct numerical simulation of a turbulent 90° bend pipe flow*. International Journal of Heat and Fluid Flow, 2018. **73**: p. 199-208.

16. Martínez, J., Lan, Y., Merzari, E., Min, M., *On the use of LES-based turbulent thermal-stress models for rod bundle simulations.* International Journal of Heat and Mass Transfer, 2019. **142**: p. 118399.

17. Maday, Y. and A. Patera. *Spectral element methods for the incompressible Navier-Stokes equations*. State of the Art Surveys in Computational Mechanics ASME, 1989, p. 71-143.

18. Fischer, P.F., Schlatter, P., *Nek5000 note*. 2005; Available: https://www.mcs.anl.gov/~fischer/nek5000/.

19. Tanaka, M., H. Ohshima, and H. Monji, *Thermal Mixing in T-Junction Piping System Related to High-Cycle Thermal Fatigue in Structure.* Journal of Nuclear Science and Technology, 2010. **47**(9): p. 790-801.

20. Tanaka, M.-a., H. Ohshima, and H. Monji, *Numerical Simulation of Thermal Striping Phenomena in a T-Junction Piping System Using Large Eddy Simulation.* Journal of Power and Energy Systems, 2009. **3**(1): p. 237-248.

21. Gnielinski, V., *Neue Gleichungen für den Wärme- und den Stoffübergang in turbulent durchströmten Rohren und Kanälen.* Forschung im Ingenieurwesen A, 1975. **41**(1): p. 8-16.